Title

Deglacial reconstruction of the spatial extent and intensity of the North Atlantic Subtropical High

Authors

David Fastovich*[1] (ORCID: 0000-0002-0340-9819)
Tripti Bhattacharya[2] (ORCID: 0000-0002-5528-3760)
Stephen T. Jackson[3] (ORCID: 0000-0002-1487-4652)
Teresa R. Krause[4] (ORCID: 0000-0003-0211-5189)
James M. Russell[5] (ORCID: ?)
Timothy M. Shanahan[6] (ORCID: 0000-0002-3831-3198)
Chijun Sun[7] (ORCID: 0000-0002-3668-346X)
John W. Williams[8] (ORCID: 0000-0001-6046-9634)

*Corresponding author, fastovich@uga.edu
[1]Department of Geography, University of Georgia, Athens, GA, USA
[2]Department of Earth and Environmental Sciences, Syracuse University, Syracuse, NY, USA
[3]National and Regional Climate Adaptation Science Centers, U.S. Geological Survey, Tucson, AZ, USA, and Department of Geosciences, University of Arizona, Tucson, AZ, USA
[4]Department of Biology, Augsburg University, Minneapolis, MN, USA
[5]Department of Earth, Environmental & Planetary Sciences, Brown University, Providence, RI, USA
[6]Department of Earth and Planetary Sciences, Jackson School of Geosciences, The University of Texas at Austin, Texas, USA
[7]Department of Earth and Planetary Sciences, University of California, Davis, Davis, CA USA
[8]Department of Geography and Center for Climatic Research, University of Wisconsin-Madison, Madison, WI, USA

Peer-review Statement

This manuscript has been submitted to *Science Advances* and is not peer-reviewed. This preprint has been submitted to EarthArXiv. Subsequent versions of this manuscript may have slightly different content. If accepted, the final version of this manuscript will be available via the 'Peer-reviewed Publication DOI' link on the right-hand side of this webpage.

CRediT (Contributor Roles Taxonomy)

David Fastovich - Conceptualization, Formal analyses, Funding acquisition, Investigation, Methodology, Project administration, Software, Validation, Visualization, Writing - original draft
Tripti Bhattacharya - Conceptualization, Funding acquisition, Investigation, Methodology, Resources, Supervision, Writing – review & editing
Stephen T. Jackson - Writing – review & editing, Investigation
Teresa R. Krause - Writing – review & editing, Investigation
James M. Russell - Writing – review & editing, Investigation
Timothy M. Shanahan - Writing – review & editing, Investigation
Chijun Sun - Writing – review & editing, Investigation
John W. Williams - Writing – review & editing, Investigation

Keywords

Hydroclimate, Leaf wax, precipitation isotopes, paleoclimate, deglaciation, atmospheric circulation

Abstract

Rainfall-related hazards are growing in southeastern North America (SENA) but well-documented climate-model biases cast doubt on projected rainfall changes. Using leaf-wax biomarkers (δD_{wax}) at White Pond, SC and Hall's Cave, TX, we reconstruct North Atlantic Subtropical High (NASH) variability across the last deglaciation (21 to 10 ka) to assess model fidelity. During the Younger Dryas, when Atlantic Ocean heat transport weakened, the NASH expanded westward, increasing rainfall in SENA. In contrast, the NASH gradually contracted eastward and weakened as deglacial greenhouse-gas concentrations increased, likely decreasing rainfall in SENA. An isotope-enabled simulation captures the first NASH response but severely underestimates the second. Because the NASH delivers moisture that drives extreme rainfall in SENA, this underestimation suggests that models cannot yet produce confident projections of regional rainfall extremes, or that those extremes will exceed current projections. Rainfall hazards facing SENA may be larger or less certain than current models suggest.

1. Introduction

Subtropical high pressure systems are a prominent feature of global atmospheric circulation and influence hydroclimate globally (*1*). Northward moisture transport along the western edge of the North Atlantic Subtropical High (NASH) is the largest moisture source in southeastern North America (SENA) (*2*, *3*) where intensifying rainfall over the coming century (*4*, *5*) threatens life, property, and economic activity. Although the largest changes are expected over coming decades, their early consequences are already evident. The cumulative cost of rainfall damages from flooding was between $39 and $91 billion from 1988 to 2017 across the United States (*6*), with the greatest rainfall increases expected in SENA (*4*). Accurate climate projections are necessary to address these accelerating challenges but coupled land-atmosphere-ocean models pose challenges for simulating precipitation in SENA. For instance, the NASH is coupled to regional and North Atlantic sea surface temperature (*1*, *7*) and the configuration of the Northern Hemisphere Hadley Cell (*8*, *9*). Substantial internal variability (e.g., North Atlantic Oscillation and Atlantic Multidecadal Variability) within each coupled component makes it difficult to isolate and identify the specific processes governing SENA hydroclimate. Constraining hydroclimate responses to different forcing mechanisms is needed to disentangle these controls and improve hydroclimate projections, which in turn requires longer-term perspectives that the instrumental record cannot provide. Disentangling these controls in SENA has implications for hydroclimate projections in other subtropical regions because subtropical highs are governed by similar ocean-atmosphere couplings globally (*1*).

The most recent deglaciation is well-suited to constrain SENA hydroclimate response to forced changes in greenhouse gases, ice sheet configuration, and ocean circulation. Following the Last Glacial Maximum, atmospheric carbon dioxide increased by ~80 ppm (*10*) which caused ice sheet loss (*11*, *12*) and subsequent ocean heat transport variability (*13*). These forcings evolved asynchronously, and included both gradual and abrupt transitions, enabling isolation of their individual effects on SENA hydroclimate. However, a lack of unambiguous hydroclimate proxies has meant that few constraints exist for deglacial hydroclimate evolution in SENA. Fossil-pollen reconstructions have been among the few empirical approaches to understanding deglacial rainfall changes in SENA (*14–16*), but both traditional (*17*) and machine-learning approaches (*18*) are limited by precipitation's secondary role in determining temperate forest composition (*19*).

Leaf wax biomarkers can constrain the patterns and drivers of SENA hydroclimate. These long-chain *n*-alkanes are readily preserved in sediments across SENA and are significantly correlated to the hydrogen isotopic signature of precipitation (δD_p) (*20*). This proxy fidelity allows the application of leaf-wax stable isotope hydroclimate reconstructions to identify changes in atmospheric circulation, moisture sources, and precipitation amount across diverse environments (*21–24*). We examine hydroclimate dynamics across the last deglaciation in SENA using the hydrogen-isotope composition of leaf-wax biomarkers from White Pond, South Carolina (34.168 °N, 80.777 °W) and Hall's Cave, Texas (30.136 °N, -99.535 °W) (*25*). Together, these two records are used to reconstruct the spatial extent and intensity of the NASH across the last deglaciation. The processes controlling deglacial evolution of the NASH are constrained with a suite of isotope-enabled climate models that provide insights into future rainfall extremes in SENA.

2. Results and Discussion

2.1 Contemporary Climatology of the North Atlantic Subtropical High and δD_p as a Tracer

Contemporary climatology indicates a close link between hydrogen isotopes in precipitation (δD_p) and upstream variability in the NASH (Figure 1). Moisture from the Gulf of Mexico is the largest source of water vapor into SENA (*3*) (Figure 1A). Zonal pressure gradients between SENA and the NASH are responsible for northward flow that delivers this moisture into SENA (Figure S1). Therefore, these northward winds and corresponding moisture advection into SENA are directly tied to the NASH.

Water vapor enriched in deuterium over the Gulf of Mexico (Figure S2) makes this moisture transport traceable in the water isotopes of precipitation (δD_p). As this water vapor is advected into SENA, the deuterium-enriched vapor produces rainfall with a distinct deuterium-enriched fingerprint across SENA (Figure 1A). Meanwhile, low meridional moisture transport in the Great Lakes, New England, and Canada indicates deuterium-depleted δD_p (Figure 1A).

The relationship between δD_p and meridional moisture transport in SENA (Figure 2B) suggests that northward transport of moisture from the Gulf of Mexico by the NASH is a primary control on SENA δD_p, overwhelming processes like distillation from continentality. For example, along a meridional transect at 88.5°W between 30–37.5°N, δD_p decreases 7‰ across 830 km of inland transport (Figure 1B). This decrease is far less than observed in other midlatitude regions such as the western United States, where δD_p decreases by 40‰ to 80‰ over 80 to 500 km (*26*, *27*) and in Europe, where δD_p decreases by 16‰ over 1,000 km (*28*) (here, we convert reported $\delta^{18}O_p$ values to δD_p, assuming equilibrium Rayleigh distillation).

2.2 A Regional Approach and Index for Reconstructing the North Atlantic Subtropical High Intensity and Extent

Northward moisture flux into SENA has an asymmetric response to variability in the spatial extent and intensity of the NASH. To quantify this variability directly from reanalysis data, we define the Bermuda High Index (BHI) as the difference in standardized mean sea level pressure between the western edge of the NASH (25.38 - 29.38 °N, 85 - 80 °W) and Great Plains (35 - 39

°N, 105.5 - 100 °W) (dashed boxes in Figure 1C, D, S1 Supplemental Information) (*29*). BHI provides an instrumental target that we aim to reconstruct.

Compositing BHI values reveals two distinct hydroclimate responses across SENA to variability in the intensity and spatial extent of the NASH (Figure 1C, D). Under a westward-expanded (BHI ≥ 90th percentile) or eastern-contracted (BHI ≤ 10th percentile) NASH, meridional moisture transport anomalies are small along the Atlantic Coastal Plain (Figure 1C, 1D). In other words, the Atlantic Coastal Plain sits within the typical spatial footprint of the NASH. Therefore, we posit that northward moisture flux into the Atlantic Coastal Plain records the *intensity* of meridional moisture transport along the western edge of the NASH. An increase in meridional moisture transport along the Atlantic Coastal Plain would increase δD_p from enhanced transport of deuterium-enriched vapor from the Gulf of Mexico (Figure S2). Meanwhile, prior analyses of δD_p in the southern Great Plains attribute decreases in δD_p to increases in stratiform rainfall from mesoscale convective systems fueled by moisture transport from the Great Plains Low Level Jet (*30*). The Great Plains Low Level Jet is coupled to the NASH through a geostrophic response to the zonal pressure gradient across the Great Plains (*25*, *31–33*). In this way, a westward expansion in the NASH leads to a large increase in northward moisture transport in the southern Great Plains (Figure 1C, 1D) and corresponding increase in the likelihood of mesoscale convective activity and decrease in δD_p (*30*). Therefore, unlike the positive relationship between the NASH, meridional moisture transport, and δD_p along the Atlantic Coastal Plain, a negative relationship is expected in the southern Great Plains. This suggests that unlike the Atlantic Coastal Plain, δD_p in the southern Great Plains is sensitive to the *spatial extent* of the NASH.

Asymmetric moisture flux responses in SENA to variability in the spatial extent and intensity of the NASH indicate that observations from both the Atlantic Coastal Plain and the southern Great Plains are needed to completely characterize the NASH, as either region alone conflates NASH intensity and spatial extent. We resolve this by taking the difference in δD_{wax} from a site in the Atlantic Coastal Plain (White Pond) and southern Great Plains (Hall's Cave) (*25*) after standardizing both records (Figure 1C, 1D, 2A, 2B), to define a leaf-wax-based reconstruction of NASH variability, $\Delta\delta D$ $NASH_{leaf\ wax}$. The resulting zonal δD_{wax} gradient reconstructs the intensity (White Pond) and spatial extent (Hall's Cave) of the NASH in a way that a single-site reconstruction cannot (Figure 1C, 1D). We reproduce $\Delta\delta D$ $NASH_{leaf\ wax}$ using ERA5 meteorological variables in place of δD_{wax}: meridional vapor transport and average rainfall rate. Both correlate significantly with mean sea level pressure over the Gulf of Mexico (reflecting NASH spatial extent) and over the western Atlantic (reflecting NASH intensity), supporting our use of zonal δD_{wax} gradients in SENA to reconstruct the spatial extent and intensity of the NASH (Figure S3).

2.3 Asymmetric North Atlantic Subtropical High response across the last deglaciation

At White Pond, δD_{wax} remains high until ~15 to 14 ka, indicating elevated transport of deuterium-enriched δD_{vapor} moisture from the Gulf of Mexico into the southeastern United States, driven by a stronger NASH. A subsequent gradual decrease in δD_{wax} at White Pond closely tracks summer insolation and ice sheet loss, suggesting a gradual decrease in northward moisture from a weakening of the NASH in response to increasing temperatures (Figure 2A). In contrast, δD_{wax} at Hall's Cave, TX demonstrates high millennial-scale variability (Figure 2B). Deglacial millennial-scale variability in the NASH wind speed has previously been shown to be inversely related to north Atlantic sea surface temperatures (*34*). The similarity between Hall's Cave δD_{wax} and north Atlantic sea surface temperatures (Figure 2B) supports this interpretation that a westward expansion of the NASH from decreased temperatures would increase stratiform rainfall and decrease δD_{wax}.

Combining White Pond and Hall's Cave δD_{wax} into a reconstruction of the intensity and spatial extent of NASH ($\Delta\delta D$ $NASH_{leaf\ wax}$, Figure 3C) identifies two distinct modes of behavior. The first mode is a weakening and contraction of the NASH in response to deglacial warming between 15.4 and 10.5 ka (Figure 2C). The second mode is an abrupt intensification and expansion in response to a weakening of the Atlantic Meridional Overturning Circulation (AMOC) that operates at millennial timescales and is particularly evident between 13.7 ka and 12 ka (Figure 2C).

Gradual weakening and contraction of the NASH in the first mode is indicated by the decrease in $\Delta\delta D$ $NASH_{leaf\ wax}$ from ~1 at 15.4 ka to ~-2 at 10.5 ka. Positive $\Delta\delta D$ $NASH_{leaf\ wax}$ between 18 ka and 15 ka reflect above-average δD_{wax} at White Pond, driven by a stronger NASH that increases the flux of deuterium-enriched Gulf of Mexico water vapor into the site (Figure 2, S4A). During this same interval Hall's Cave δD_{wax} is below average from increased stratiform rainfall, fueled by elevated Gulf of Mexico moisture transport, thereby increasing the zonal δD_{wax} gradient across SENA (Figure 2, S4G). Collectively, these site-level changes, summarized in $\Delta\delta D$ $NASH_{leaf\ wax}$, suggest that the late-glacial (18 ka to 15 ka) NASH was stronger and larger relative to the Holocene (11 ka to 10 ka). The NASH weakened after ~15 ka as White Pond δD_{wax} decreased below mean values and contracted eastward as Hall's Cave δD_{wax} increased above mean values (Figure S4). High moisture flux between 18 ka and 15 ka suggests elevated late-glacial precipitation that declined into the Holocene.

Large Northern Hemisphere ice loss at ~15 ka may explain the long-term NASH weakening and contraction inferred from $\Delta\delta D$ $NASH_{leaf\ wax}$ (Figure 2A, 2B, 2C). Northern Hemisphere ice loss would have decreased albedo and reduced the Northern Hemisphere meridional temperature gradient, weakening Hadley Cell subsidence in the subtropics and the NASH. This proposed mechanism is consistent with Last Glacial Maximum climate model experiments, in which high albedo produces an intensified NASH (*35*).

An abrupt increase in the $\Delta\delta D$ $NASH_{leaf\ wax}$ to ~1 near the Younger Dryas suggests a westward expansion of the NASH caused by cooling of north Atlantic sea surface temperatures from a reduction in the AMOC (Figure 2B, 2C, 2D). A westward expansion decreases δD_{wax} at Hall's Cave below mean values from increased stratiform rainfall fueled by concentrated moisture transport toward Hall's Cave from an expanded NASH, increasing $\Delta\delta D$ $NASH_{leaf\ wax}$ (Figure 2C, S4G). Notably, White Pond δD_{wax} shows no abrupt deviation across the Younger Dryas, suggesting NASH intensity did not change appreciably during this interval, only its spatial extent (Figure 2C, S4A). This NASH configuration would have driven enhanced northward moisture transport along an expanded western flank of the NASH and increased precipitation in the Great Plains consistent with increased hydroclimate-sensitive tree taxa abundance at Cupola Pond, MO between ~13 and ~11 ka (*25*).

The North Atlantic Oscillation has long served as analogue for interpreting patterns of Atlantic temperature and atmospheric circulation change during reductions of AMOC strength (*34*, *36*, *37*), in part because direct proxy evidence of changes in the NASH or the Icelandic Low has been lacking. $\Delta\delta D$ $NASH_{leaf\ wax}$ directly probes the intensity and spatial extent of NASH and clarifies that the NASH may not only have intensified as previously inferred (*34*, *36*, *37*), but also expanded westward (Figure 2). Alternatively, the NASH may have expanded westward without intensification.

An intensification and expansion, or a westward expansion alone, of the NASH is likely linked to changes in the Northern Hemisphere meridional temperature gradient, the same mechanism proposed for the greenhouse-gas-driven weakening of the NASH. The two responses differ in pace because deglacial AMOC perturbations were abrupt (Figure 2D), while ice sheet loss was gradual and monotonic (Figure 2A). During the Younger Dryas, a weakening of the AMOC abruptly cooled SSTs in the north Atlantic from reduced ocean heat transport (Figure 2B) which would have increased the Northern Hemisphere meridional temperature gradient, Hadley circulation subsidence (*38*), and the NASH. In addition, lower SSTs may have directly increased NASH intensity and spatial extent by increasing air density and mean sea level pressure. However, Heinrich Event 1 likely had a larger reduction in the AMOC (*13*), yet $\Delta\delta D$ $NASH_{leaf\ wax}$ suggests little change to the NASH (Figure 2C, 2D). We propose that the sensitivity of NASH extent to AMOC perturbations depends on background climate state. Under nearly full-glacial boundary conditions (as during Heinrich Event 1), the NASH response is muted, whereas under intermediate conditions (as during the Younger Dryas), the NASH response is pronounced. This may be because sea ice extent was already extensive before Heinrich event cooling initiated (*39*).

2.4 Simulations of the North Atlantic Subtropical High and Proxy-Model Comparisons

To assess our proxy-inferred NASH reconstruction ($\Delta\delta D$ $NASH_{leaf\ wax}$) and its causal mechanisms, we examine a suite of isotope-enabled Community Earth System Model (iCESM) experiments. Within these experiments we reproduce ΔδD $NASH_{leaf\ wax}$ with simulated δD_p by taking the standardized difference between simulated δD_p for the four grid cells surrounding White Pond and Hall's Cave, to define ΔδD $NASH_{iCESM}$. We distinguish the proxy reconstruction (ΔδD $NASH_{leaf\ wax}$) from its model analogue (ΔδD $NASH_{iCESM}$) using subscripts. For each iCESM experiment we take the difference between high (≥ 90th percentile) and low ΔδD $NASH_{iCESM}$ years (≤ 10th percentile), which demonstrate that the zonal δD_p gradient across SENA appears closely coupled with the NASH (Figure 3).

In a simulation from 1979-2023 nudged to ERA5 reanalysis (WisoMIP) (*40*) and an un-nudged simulation of the last millennium (iLME, 850 to 2006) (*41*, *42*), the zonal δD_p gradient increases as expected when the NASH expands westward, in agreement with our contemporary δD_p analyses and δD_{wax} proxy inferences (Figure 3A, 3B). However, in a transient, deglacial simulation (iTRACE) with greenhouse gas, ice sheet extent, ocean heat transport, and orbital forcings derived from proxy observations (*43*), the simulated zonal δD_p gradient across SENA increases when the NASH weakens and contracts eastward: an opposite relationship to our proxy records (Figure 3D). These findings indicate that iCESM1 accurately simulates the relationship between the zonal δD_p gradient in SENA and the NASH, but that the model struggles when forcings beyond those of the last millennium or historical period are introduced. This modeling challenge is caused, in part, by the response of the Intertropical Convergence Zone to the AMOC which is erroneously linked to meridional moisture flux and corresponding δD_p at Hall's Cave in iTRACE (Supplementary Information).

Despite these modeling challenges, iTRACE partly simulates the response of the NASH to a weakening of the AMOC. Applying the same BHI defined from reanalysis (Section 2.2) to iTRACE's simulated pressure fields, enables comparing the simulated NASH to ΔδD $NASH_{leaf\ wax}$. The simulated NASH matches the millennial-scale variability in ΔδD $NASH_{leaf\ wax}$ (Figure 4), which propagates to simulated integrated vapor transport and δD_p. High BHI values between 18 ka and 14 ka demonstrates that the NASH intensified and expanded westward, which increased simulated moisture flux at White Pond (Figure 4C, 4D). These coupled changes between simulated meridional vapor transport at White Pond and BHI appear linked to simulated sea surface temperatures in the North Atlantic (Figure 4E), and therefore the AMOC. Low North Atlantic sea surface temperatures force an intensification and expansion of the NASH, indicated by high BHI values, with downstream increases in meridional vapor transport at White Pond (Figure 4C, 4D, 4E). Critically, however, iTRACE fails to simulate a gradual weakening of the NASH, because BHI values for the Holocene (12 ka to 11 ka) are nearly identical to the late-glacial (20 ka to 19 ka) (Figure 4D).

This failure carries a troubling implication when extended to future extreme rainfall projections. Current projections indicate that the extreme rainfall is likely to become more common in SENA (*4*), with increases in SENA fall rainfall already linked to variability in the NASH (*44*). Yet, iTRACE reveals that models dramatically underestimate the NASH response to greenhouse gas increases, and therefore the moisture flux that supplies rainfall (Figure S4C, S4D, S4E). Since extreme rainfall scales with mean rainfall rates (*45*) and meridional moisture flux is a key ingredient for extreme rainfall in SENA (*46*), iTRACE is likely also underestimating past extreme rainfall. When placed alongside current extreme rainfall projections, our results support two conclusions. In the best case, ESMs may not produce confident projections of regional extreme rainfall. In the worst case, extreme rainfall in SENA may exceed latest ESM projections because these very models underestimate the NASH response in the past.

3. Conclusions

Our results demonstrate that the zonal δD_p and δD_{wax} gradient across SENA records changes in moisture delivered by the NASH to the region. Using this regional gradient, we show that the NASH weakened and contracted in response to gradual warming across the last deglaciation, which likely drove gradual drying in SENA. However, the NASH intensified in response to a weakening in Atlantic Ocean heat transport, increasing precipitation in SENA. A transient, isotope-enabled climate model experiment (iTRACE) accurately simulates the responses of the NASH to a weakening of ocean heat transport, but underestimates responses to gradual deglacial warming. Because Northern Hemisphere subtropical highs are expected to strengthen into the future (*47*), leading to increases in projected rainfall extremes in SENA (*4*), the inability of iTRACE to accurately simulate the response of the NASH to greenhouse-gas induced warming suggests that past and future simulations of extreme rainfall are poorly constrained and possibly underestimated. Future rainfall hazards may be less certain, and substantially larger, than currently projected.

Acknowledgements

We gratefully acknowledge technical support from the Georgia Advanced Computing Resource Center and Stephanie Bullinger (Syracuse University). DF and TB acknowledge funding support from the National Science Foundation award AGS-2402498. TB acknowledges support from NSF CAREER Grant OCE-2237502 and Sloan Foundation Fellowship FG-2023-20259. White Pond was cored with support from NSF DEB-1353896. Initial lipid extraction at White Pond was supported by NSF DEB-1349662 and leaf wax biomarker measurements were made possible with support from NSF MRI Grant EAR-2018078.

Source Data

All data, including derived iCESM fields (integrated vapor transport), along with analysis code and a containerized computing environment, are available on Zenodo (*48*). The original iCESM model output is not included due to its size but freely available from the National Science

Foundation National Center for Atmospheric Research Geoscience Data Exchange (*49*, *50*) and the NASA Center for Climate Simulation (*40*). White Pond, SC δD_{wax} measurements are also freely accessible on the NOAA Paleoclimatology Database and Zenodo (*48*). Hall's Cave, TX δD_{wax} is also accessible in the supplemental information of the original publication (*25*).

4. Materials and Methods

4.1 Leaf wax analyses and δD_{wax} measurements

White Pond, SC was cored in April 2015 using a modified Livingstone square-rod piston corer, from which 5.85 meters of sediment were retrieved (*51*). Sediments were subsampled and processed using standard organic geochemical approaches to extract, purify, quantify, and measure leaf wax biomarkers in two stages. In 2015, sediments were first freeze-dried, homogenized, and all lipid compounds were extracted using a Dionex ASE 350 and a 9:1 mixture of dichloromethane:methanol. The total lipid extract was separated into apolar and polar fractions using alumina columns with 9:1 hexane:dichloromethane and 1:1 dichloromethane:methanol as eluents, respectively. The polar fraction was then filtered, and branched glycerol dialkyl glycerol tetraethers were identified and quantified in 2016 (*52*). The apolar fraction was then dried and stored.

In 2025, the apolar fraction was further processed to isolate *n*-alkane leaf waxes. We first added a known quantity of 5α-androstane to aid in quantifying leaf wax biomarkers. We then performed an additional, polarity-based separation using 5% deactivated silica gel columns to separate leaf wax *n*-alkanes (apolar alkyl lipids) from mildly polar compounds (e.g. ketone compounds). *n*-alkanes were eluted with hexane, and mildly polar compounds were eluted using dichloromethane. The isolated *n*-alkane leaf waxes were then quantified using a Thermo TRACE-1310 gas chromatograph with a programmable temperature vaporization inlet and a flame ionization detector. Once quantified, we measured the hydrogen and carbon isotopic composition of C_{31} and C_{27} leaf-waxes using a Delta V Plus isotope ratio mass spectrometer in continuous flow mode (Conflo IV) coupled to a Thermo TRACE-1310 through a GC-Isolink II. All samples were measured in duplicate to achieve a precision better than 2‰ for C_{31} δD_{wax} and 0.2‰ for C_{31} $\delta^{13}C_{wax}$. A synthetic *n*-alkane mix (A7 mix from Arndt Schimmelmann at Indiana University) was measured at regular intervals in between samples to monitor instrument drift and correct for any apparent offsets.

We assessed the fidelity of our δD_{wax} measurements at White Pond, SC to record δD_p with a core-top sample. For this core-top sample, we also measured $\delta^{13}C_{wax}$ to correct for biosynthetic fractionation. We applied a two-end-member Bayesian mixing model to correct for leaf wax biosynthesis fractionation processes (*53*), yielding an estimate of δD_p. For C_{31} alkanes, the reconstructed δD_p median estimate is -34.57‰ (95% CI: -40.12, -28.28) while the Online

Isotopes in Precipitation Calculator (OIPC) (*54*) estimates an annual value of -28.43‰ (p = 0.058, Figure S5). In contrast, C_{27} the δD_p reconstruction has a median estimate of -37.36‰ (95% CI: -42.73, -31.31). We perform all analyses on C_{31} leaf waxes because the core-top δD_p estimate more closely matches OIPC (Figure S5).

δD_{wax} measurements from Hall's Cave, TX were downloaded from the original publication (Supplementary Data 1 in (*25*)) in February 2026. Only C_{27} δD_{wax} measurements are available for Hall's Cave; therefore, we replicate our analyses using C_{27} δD_{wax} measurements from White Pond and find high agreement (Figure S6) suggesting our conclusions are insensitive to this analytical choice.

4.2 ΔδD NASH$_{\text{leaf wax}}$ Calculation

We reconstructed variability in the North Atlantic Subtropical High across the last deglaciation using δD_{wax} measurements from White Pond, SC and Hall's Cave, TX and propagated temporal and measurement uncertainties using a Monte Carlo approach. We first generated new Bayesian age models for both sites using *Bacon* (*55*) and the chronological controls reported in each publication (*25*, *52*). For White Pond, we used the parameters in the original publication (*52*). These parameters were not recorded for Hall's Cave, so we use the default recommendations from *Bacon*. All *Bacon* parameters and corresponding code are freely available for review (*48*). We then defined a common temporal grid for interpolating δD_{wax}, spanning the overlapping age range of both records with a time step equal to the median temporal resolution across both sites.

To generate an ensemble of interpolated δD_{wax} records, we first propagated measurement uncertainty by randomly resampling δD_{wax} from $N\left(\mu_{\text{wax}},\ \frac{\sigma_{\text{wax}}}{\sqrt{N}}\right)$, where $N = 2$, reflecting duplicate measurements at both sites. At White Pond, μ_{wax} and σ_{wax} were estimated from the duplicate measurements directly. Individual σ_{wax} values were not reported for Hall's Cave, so we assigned $\sigma_{\text{wax}} = 5$ based on measurement uncertainties described in the original publication and assume that reported δD_{wax} values estimate μ_{wax} (*25*). Each resampled δD_{wax} record was then interpolated to the common temporal grid using age estimates drawn randomly from the posterior ensemble of the *Bacon* age models. Repeating this process 1,000 times produced an ensemble of interpolated δD_{wax} records that incorporate both age and measurement uncertainties. We standardized each ensemble member and subtracted the Hall's Cave ensemble from the White Pond ensemble, yielding 1,000 estimates of ΔδD NASH$_{\text{leaf wax}}$, from which we report the median and 95% confidence interval.

4.3 Climate simulations and contemporary climate data products

We examine the transient, deglacial isotope-enabled iTRACE experiments (*43*) to identify the dynamics of hydroclimate variability in ENA. The iTRACE experiments attempt to simulate climate evolution during the last deglaciation with the isotope-enabled Community Earth System Model v1.2 (iCESM). These simulations include transient changes in greenhouse gas concentrations, orbital configuration, ice sheets, and meltwater from 20,000 years before present (ka) to 11 ka. Simulations were performed at a nominal 2° horizontal resolution for the atmosphere and land model and 1° horizontal resolution for the ocean and sea ice models, with 30 vertical layers in the atmosphere.

The transient iTRACE experiments are compared against the iCESM simulations from Water Isotope Model Intercomparison Project (iCESM v1.3, WisoMIP) (*40*) experiments and the isotope-enabled Last Millennium Ensemble (iCESM v1, iLME) (*40*–*42*) to examine the sensitivity of the zonal δD_p gradient in southeastern North American to the North Atlantic Subtropical High. The WisoMIP simulations span 1979-2023 and are performed with only the atmosphere component of iCESM1.3 (i.e. iCAM5). Sea ice, sea surface temperatures, zonal and meridional winds, and atmospheric temperature were prescribed from ERA5 reanalysis throughout the simulation. This nudging corrects model biases and isolates the representation of isotope systematics within iCESM1.3 (*40*). iLME spans the last 1,000 years (850 to 2006 CE) with transient solar intensity, volcanic emissions, greenhouse gases, aerosols, land use conditions, and orbital parameters as forcings (*41*, *42*). Unlike WisoMIP, iLME is coupled to an ocean model and not nudged to correct for model biases. Both simulations were performed with a horizontal and vertical resolution comparable to iTRACE (*41*, *42*). Together, this suite of simulations lets us assess whether mean-state biases or the response to forcings drive misrepresentation of the zonal δD_p gradient–North Atlantic Subtropical High relationship.

Within all models we calculate the integrated vapor transport as:

$$\mathbf{IVT} = \frac{1}{g}\int_{p_{\mathrm{top}}}^{p_{\mathrm{sfc}}} q\,\mathbf{V}\,dp$$

Where **V** is horizontal winds, q is specific humidity, g is gravitational acceleration, p is pressure, p_s is surface pressure, and p_{top} is top of the atmosphere pressure.

4.3.1 Reconciling the inverse δD_p gradient-North Atlantic Subtropical High relationship in iTRACE

Unlike evidence from our proxy records, WisoMIP, and iLME, which demonstrate that an intensification and expansion of the North Atlantic Subtropical High increases the zonal $\delta D_p/\delta D_{wax}$ gradient in southeastern North America (Figure 4), the simulated δD_p gradient in iTRACE (Figure 3) has an antiphase relationship to the North Atlantic Subtropical High. That is, an increase in the simulated zonal δD_p gradient in southeastern North America occurs when the North Atlantic Subtropical High has weakened and contracted (Figure 4C, S9). Composites comparing intervals of high (≥ 90th percentile) and low (≤ 10th percentile) $\Delta\delta D$ $NASH_{iCESM}$ in iTRACE reinforce that the δD_p gradient in southeastern North America is still tied to a large-scale atmospheric reorganization centered on the North Atlantic (Figure 4C, S9). However, periods with a high zonal δD_p gradient in southeastern North America represent time intervals with a northward shift in the Intertropical Convergence Zone (e.g. Bølling-Allerød and Holocene) in response to a resumption of the Atlantic Meridional Overturning Circulation and a subsequent increase in North Atlantic temperature (Figure S7, S8). As the Intertropical Convergence Zone shifts northward following anomalously high temperatures in the North Atlantic (Figure S7, S8), positive precipitation anomalies in the subtropics decrease δDp through the 'amount effect' (Figure S8)(*56*). A northward shift in the Intertropical Convergence Zone also produces easterly integrated vapor transport anomalies in the tropics. These anomalies transmit the negative δD_p signal to Hall's Cave, increasing the zonal δDp gradient in southeastern North America (Figure 4D, S8). Since the Bølling-Allerød and Holocene represent increases in northern subtropical Atlantic temperatures (Figure S7), the North Atlantic Subtropical High weakens, likely from enhanced atmospheric column thickness over the northern subtropical Atlantic relative to subpolar North Atlantic (Figure S8). Hence, the erroneous connection between the Intertropical Convergence Zone and Hall's Cave forces an increase in the zonal δD_p gradient in southeastern North America despite a weakening and contraction of the North Atlantic Subtropical High (Figure S9, S10).

4.4 North Atlantic Subtropical High definition and metrics

Within iTRACE, we examine variability in the North Atlantic Subtropical High using a modified version of the Bermuda High Index (BHI) from (*29*). The BHI is defined as the area weighted difference in mean sea level pressure between the Gulf of Mexico (25.38 - 29.38 °N, 95 - 90 °W) and the southern Great Plains (35 - 39 °N, 105.5 - 100 °W) and is designed, in part, to capture westward expansions in the North Atlantic Subtropical High (*29*). For instance, an intensification and westward expansion of the North Atlantic Subtropical High increases both the pressure gradient and the BHI, driving stronger northward winds into southeastern North America. To account for climate model mean-state biases in north Atlantic sea surface temperatures and corresponding mean sea level pressure across our different iCESM experiments and ERA5, we shift the Gulf of Mexico region five degrees east. That is, we define the Gulf of Mexico mean sea level pressures as the area weighted average between 25.38 - 29.38 °N, 85 - 80 °W (Figure 1). In addition, we standardize mean sea level pressure before taking the difference between the Gulf of Mexico and Great Plains to put both locations on a common scale, allowing both to equally contribute to the BHI.

Figures

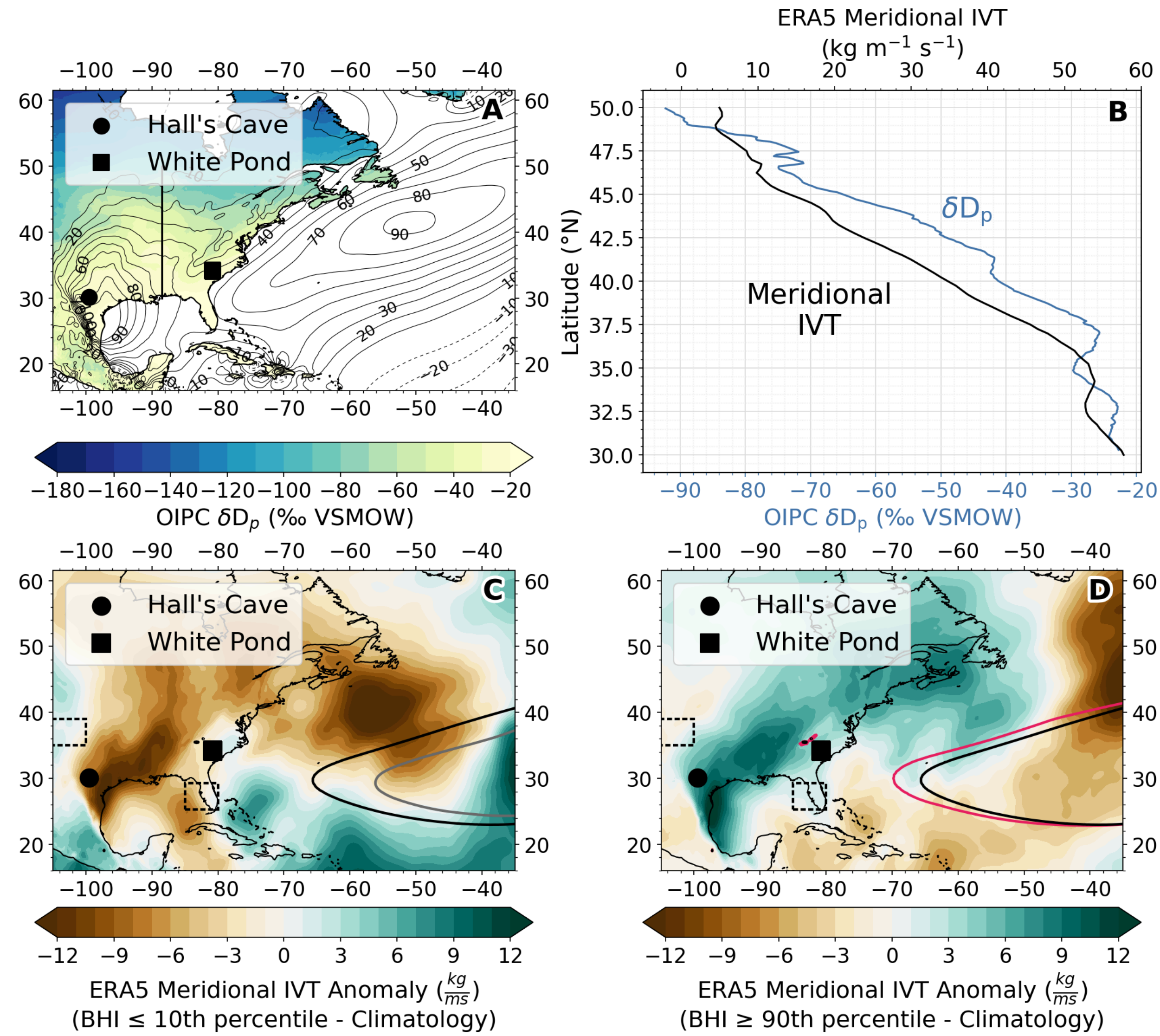

Figure 1. The relationship between meridional moisture transport, δD_p, and the North Atlantic Subtropical High in southeastern North America, and the contrasting signals recorded by Hall's Cave and White Pond during shifts in North Atlantic Subtropical High spatial extent. (A) The contemporary climatology of δD_p in SENA, where the filled contours correspond to δD_p and the black contours correspond to meridional integrated vapor transport from ERA5 with the 0 contour omitted. The black vertical line shows the transect presented in B. (B) A latitudinal transect at 88.5°W of integrated vapor transport (black line) and δD_p (blue line) between 30°and 50°N. δD_p values are from the Online Isotopes in Precipitation Calculator (*54*). (C) Map of meridional integrated vapor transport anomalies (filled contours) for an eastward contraction (BHI ≤ 10th percentile) of the North Atlantic Subtropical High relative to the 1940 to 2024 average. The black contour corresponds to the climatological position of the 1019 hPa isobar, while the gray contour corresponds to the 1019 hPa isobar under an eastward contraction of the North Atlantic Subtropical High. D) As in C but for an westward expansion with the pink

contour corresponding to the 1019 hPa isobar under an westward expansion of the North Atlantic Subtropical High (BHI ≥ 90th percentile) of the North Atlantic Subtropical High. Black dashed boxes in (C) and (D) correspond to the regions used to calculate BHI. In all mapped panels, the circle indicates Hall's Cave and the square indicates White Pond; these sites record contrasting signals during shifts in North Atlantic Subtropical High intensity and spatial extent.

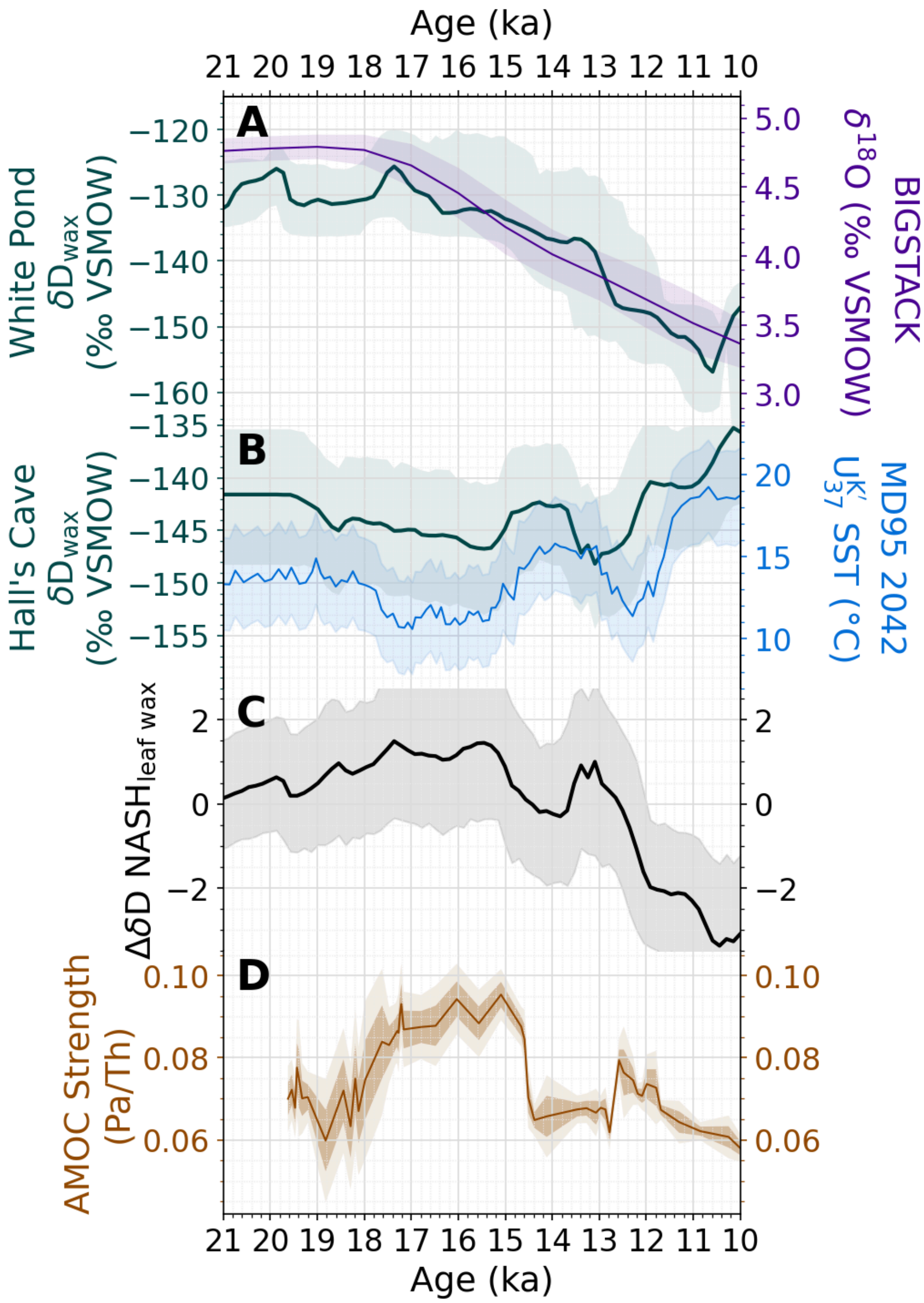

Figure 2. North Atlantic Subtropical High evolution during the last deglaciation. (A) Median White Pond δD_{wax} (green line, green shading represents the 95% CI) from a resampling approach that propagates measurement and temporal uncertainty compared benthic foraminifera $\delta^{18}O$, a proxy for global ice volume (purple line, purple shading represents 1-σ measurement and temporal uncertainty) (*57*). (B) As in (A), but for Hall's Cave δD_{wax}, plus reconstructed north Atlantic sea surface temperatures from MD95 2042 (*58*) (shading representing the 95% CI). (C) Median $\Delta\delta D$ $NASH_{leaf\ wax}$ values calculated as the standardized difference in δD_{wax} between White Pond and Hall's Cave (black line, gray shading represents the 95% CI), with temporal and measurement uncertainty propagated. (D) Reconstructed AMOC variability based on Pa/Th ratios in sediment cores from Bermuda Rise (*13*), with larger values representing a weaker AMOC (dark and light shading represent the 1-σ and 2-σ measurement uncertainty, respectively). A map of all site is present in the Supplemental Information (Figure S11).

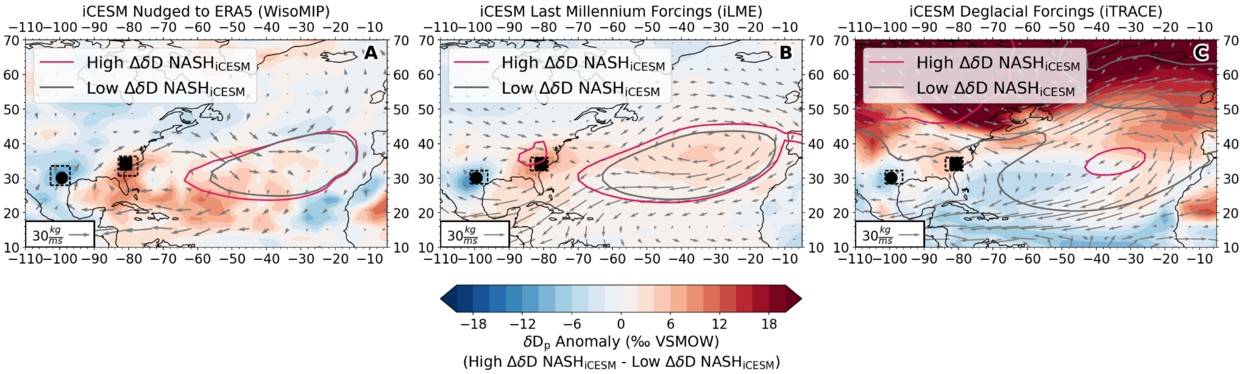

Figure 3. Isotopic fingerprint of the North Atlantic Subtropical High. Composites of mean sea level pressure (contours), integrated vapor transport (vectors), and δD_p (filled contours) from three iCESM experiments for high (≥ 90th percentile) - low (≤ 10th percentile) $\Delta\delta D$ NASH$_{iCESM}$ years (*40–43*). $\Delta\delta D$ NASH$_{iCESM}$ is defined identically to $\Delta\delta D$ NASH$_{leaf\ wax}$: the standardized difference between the four grid cells bounding White Pond and Hall's Cave simulated δD_p. For each experiment, the integrated vapor transport vectors and δD_p filled contours show the anomaly between high-$\Delta\delta D$ NASH$_{iCESM}$ and low-$\Delta\delta D$ NASH$_{iCESM}$ years. In contrast, the pink contour shows mean sea level pressure during high-$\Delta\delta D$ NASH$_{iCESM}$ years, while the gray contour shows mean sea level pressure during low-$\Delta\delta D$ NASH$_{iCESM}$ years, so the two contours together reveal how the simulated North Atlantic Subtropical High shifts in spatial extent and intensity. Note, given the different underlying boundary conditions we present the 1020 hPa contour in (A) and (B), but the 1030 hPa contour in (C).

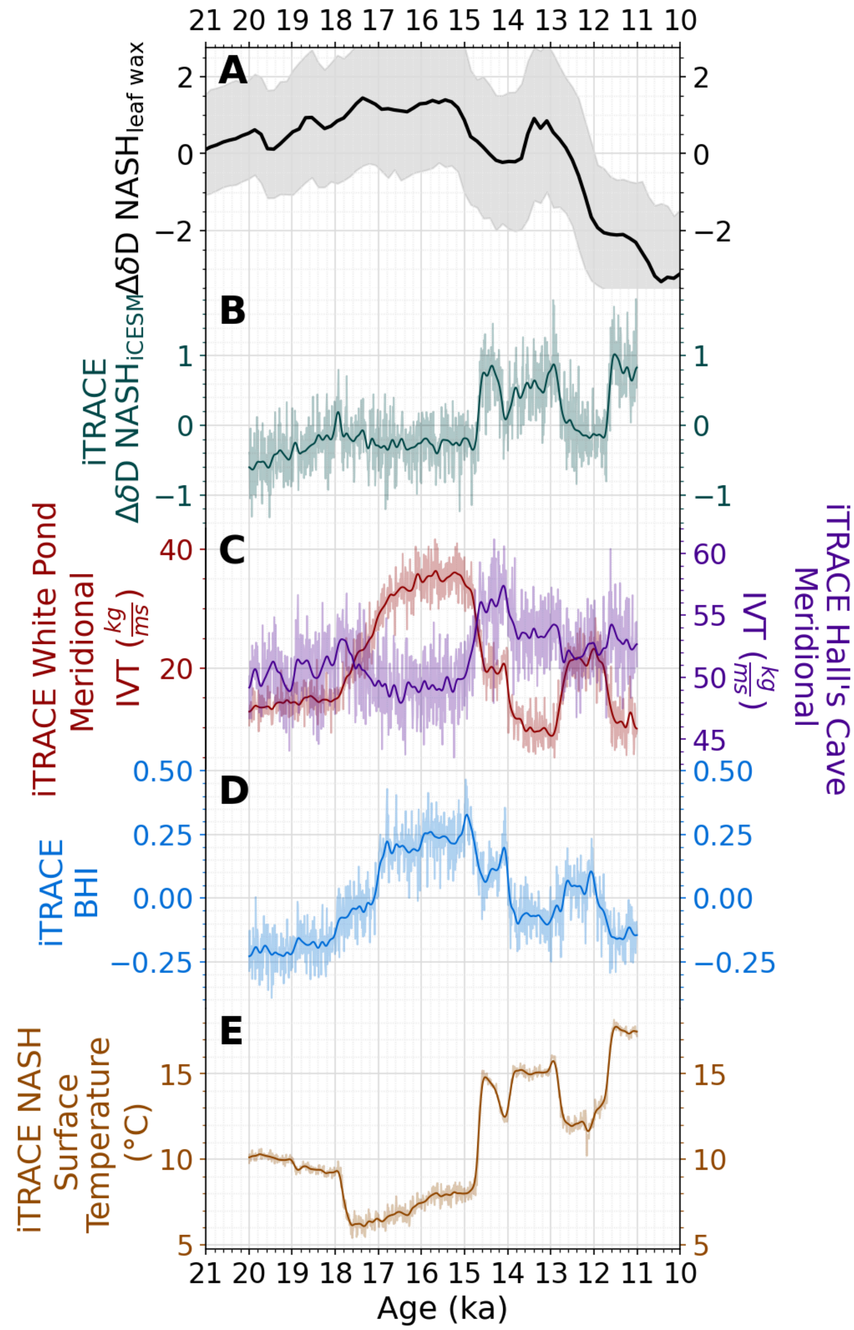

Figure 4. iTRACE deglacial hydroclimate dynamics. (A) Median ΔδD $NASH_{leaf\ wax}$ values calculated as the standardized difference in δD_{wax} between White Pond and Hall's Cave (black line, gray shading represents the 95% CI), with temporal and measurement uncertainty propagated. (B) ΔδD $NASH_{iCESM}$ calculated identically to (A) but from simulated δD_p for the four grid cells bounding White Pond and Hall's Cave from iTRACE. (C) Simulated meridional integrated vapor transport at White Pond (red line) and Hall's Cave (purple line). (D) Simulated iTRACE BHI, as used in Figure 1C and 1D. (E) Simulated North Atlantic iTRACE sea surface temperature, averaged between 35° to 40°N and 55° to 65°W. In panels B to E the light lines correspond to decadal averages and the dark lines correspond to a Gaussian low-pass filter (σ = 50 years).

References

1. M. J. Rodwell, B. J. Hoskins, Subtropical Anticyclones and Summer Monsoons. *J. Clim.* **14**, 3192–3211 (2001).

2. G. S. Benton, M. A. Estoque, Water-vapor transfer over the North American continent. *J. Atmospheric Sci.* **11**, 462–477 (1954).

3. E. M. Rasmusson, Atmospheric water vapor transport and the water balance of North America: Part I. Characteristics of the water vapor flux field. *Mon. Weather Rev.* **95**, 403–426 (1967).

4. D. R. Easterling, K. E. Kunkel, J. R. Arnold, T. Knutson, A. N. LeGrande, L. R. Leung, "Precipitation change in the United States" in *Climate Science Special Report: A Sustained Assessment Activity of the U.S. Global Change Research Program*, D. J. Wuebbles, D. W. Fahey, K. A. Hibbard, D. J. Dokken, B. C. Stewart, T. K. Maycock, Eds. (U.S. Global Change Research Program, Washington, D.C., USA, 2017)vol. I, pp. 207–230.

5. J. Zhao, T. Y. Gan, G. Zhang, S. Zhang, Projected changes of precipitation extremes in North America using CMIP6 multi-climate model ensembles. *J. Hydrol.* **621**, 129598 (2023).

6. F. V. Davenport, M. Burke, N. S. Diffenbaugh, Contribution of historical precipitation change to US flood damages. *Proc. Natl. Acad. Sci.* **118**, e2017524118 (2021).

7. H. M. Hasanean, Variability of the North Atlantic subtropical high and associations with tropical sea-surface temperature. *Int. J. Climatol.* **24**, 945–957 (2004).

8. R. Grotjahn, *Global Atmospheric Circulations: Observations and Theories* (Oxford university press, New York Oxford, 1993).

9. W. Qiu, M. Collins, A. A. Scaife, Winter Subtropical Highs, the Hadley Circulation and Baroclinic Instability. *J. Geophys. Res. Atmospheres* **128**, e2023JD039604 (2023).

10. S. A. Marcott, T. K. Bauska, C. Buizert, E. J. Steig, J. L. Rosen, K. M. Cuffey, T. J. Fudge, J. P. Severinghaus, J. Ahn, M. L. Kalk, J. R. McConnell, T. Sowers, K. C. Taylor, J. W. C. White, E. J. Brook, Centennial-scale changes in the global carbon cycle during the last deglaciation. *Nature* **514**, 616 (2014).

11. P. U. Clark, J. D. Shakun, P. A. Baker, P. J. Bartlein, S. Brewer, E. J. Brook, A. E. Carlson, H. Cheng, D. S. Kaufman, Z. Liu, T. M. Marchitto, A. C. Mix, C. Morrill, B. L. Otto-Bliesner, K. Pahnke, J. M. Russell, C. Whitlock, J. F. Adkins, J. L. Blois, J. Clark, S. M. Colman, W. B. Curry, B. P. Flower, F. He, T. C. Johnson, J. Lynch-Stieglitz, V. Markgraf, J. F. McManus, J. X. Mitrovica, P. I. Moreno, J. W. Williams, Global climate evolution during the last deglaciation, *Proceedings of the National Academy of Sciences*. **109** (2012)pp. E1134–E1142.

12. A. S. Dalton, M. Margold, C. R. Stokes, L. Tarasov, A. S. Dyke, R. S. Adams, S. Allard, H. E. Arends, N. Atkinson, J. W. Attig, P. J. Barnett, R. L. Barnett, M. Batterson, P.

Bernatchez, H. W. Borns, A. Breckenridge, J. P. Briner, E. Brouard, J. E. Campbell, A. E. Carlson, J. J. Clague, B. B. Curry, R.-A. Daigneault, H. Dubé-Loubert, D. J. Easterbrook, D. A. Franzi, H. G. Friedrich, S. Funder, M. S. Gauthier, A. S. Gowan, K. L. Harris, B. Hétu, T. S. Hooyer, C. E. Jennings, M. D. Johnson, A. E. Kehew, S. E. Kelley, D. Kerr, E. L. King, K. K. Kjeldsen, A. R. Knaeble, P. Lajeunesse, T. R. Lakeman, M. Lamothe, P. Larson, M. Lavoie, H. M. Loope, T. V. Lowell, B. A. Lusardi, L. Manz, I. McMartin, F. C. Nixon, S. Occhietti, M. A. Parkhill, D. J. W. Piper, A. G. Pronk, P. J. H. Richard, J. C. Ridge, M. Ross, M. Roy, A. Seaman, J. Shaw, R. R. Stea, J. T. Teller, W. B. Thompson, L. H. Thorleifson, D. J. Utting, J. J. Veillette, B. C. Ward, T. K. Weddle, H. E. Wright, An updated radiocarbon-based ice margin chronology for the last deglaciation of the North American Ice Sheet Complex, *Quaternary Science Reviews*. **234** (2020)p. 106223.

13. J. F. McManus, R. Francois, J. M. Gherardi, L. D. Keigwin, S. Brown-Leger, Collapse and rapid resumption of Atlantic meridional circulation linked to deglacial climate changes. *Nature* **428**, 834–837 (2004).

14. D. Fastovich, J. M. Russell, S. A. Marcott, J. W. Williams, Spatial fingerprints and mechanisms of precipitation and temperature changes during the Younger Dryas in eastern North America. *Quat. Sci. Rev.* **294**, 107724 (2022).

15. J. S. Salonen, F. Schenk, J. W. Williams, B. Shuman, A. L. Lindroth Dauner, S. Wagner, J. Jungclaus, Q. Zhang, M. Luoto, Patterns and drivers of Holocene moisture variability in mid-latitude eastern North America. *Nat. Commun.* **16**, 3582 (2025).

16. B. N. Shuman, J. Marsicek, W. W. Oswald, D. R. Foster, Predictable hydrological and ecological responses to Holocene North Atlantic variability. *Proc. Natl. Acad. Sci.* **116**, 5985–5990 (2019).

17. M. Chevalier, B. A. S. Davis, O. Heiri, H. Seppa, B. M. Chase, K. Gajewski, T. Lacourse, R. J. Telford, W. Finsinger, J. Guiot, N. Kuhl, S. Y. Maezumi, J. R. Tipton, V. A. Carter, T. Brussel, L. N. Phelps, A. Dawson, M. Zanon, F. Valle, C. Nolan, A. Mauri, A. de Vernal, K. Izumi, L. Holmstrom, J. Marsicek, S. Goring, P. S. Sommer, M. Chaput, D. Kupriyanov, Pollen-based climate reconstruction techniques for late Quaternary studies. *Earth-Sci. Rev.* **210**, 33 (2020).

18. J. S. Salonen, M. Korpela, J. W. Williams, M. Luoto, Machine-learning based reconstructions of primary and secondary climate variables from North American and European fossil pollen data. *Sci Rep* **9**, 13 (2019).

19. S. Juggins, Quantitative reconstructions in palaeolimnology: new paradigm or sick science? *Quat. Sci. Rev.* **64**, 20–32 (2013).

20. D. Sachse, I. Billault, G. J. Bowen, Y. Chikaraishi, T. E. Dawson, S. J. Feakins, K. H. Freeman, C. R. Magill, F. A. McInerney, M. T. J. van der Meer, P. Polissar, R. J. Robins, J. P. Sachs, H. L. Schmidt, A. L. Sessions, J. W. C. White, J. B. West, A. Kahmen, "Molecular Paleohydrology: Interpreting the Hydrogen- Isotopic Composition of Lipid Biomarkers from Photosynthesizing Organisms" in *Annual Review of Earth and Planetary Sciences, Vol*

40, R. Jeanloz, Ed. (Annual Reviews, Palo Alto, 2012)vol. 40 of *Annual Review of Earth and Planetary Sciences*, pp. 221–249.

21. T. Bhattacharya, J. E. Tierney, P. DiNezio, Glacial reduction of the North American Monsoon via surface cooling and atmospheric ventilation. *Geophys. Res. Lett.* **44**, 5113–5122 (2017).

22. D. Fastovich, T. Bhattacharya, L. C. Pérez-Ángel, N. J. Burls, R. Feng, S. Knapp, T. Mayer, Large-scale sea surface temperature gradients govern westerly moisture transport in western Ecuador during the Plio-Pleistocene. *Earth Planet. Sci. Lett.* **640**, 118781 (2024).

23. S. J. Feakins, Pollen-corrected leaf wax D/H reconstructions of northeast African hydrological changes during the late Miocene. *Palaeogeogr. Palaeoclimatol. Palaeoecol.* **374**, 62–71 (2013).

24. J. E. Tierney, J. M. Russell, Y. S. Huang, J. S. S. Damste, E. C. Hopmans, A. S. Cohen, Northern hemisphere controls on tropical southeast African climate during the past 60,000 years. *Science* **322**, 252–255 (2008).

25. C. Sun, T. M. Shanahan, P. N. DiNezio, N. P. McKay, P. D. Roy, Great Plains storm intensity since the last glacial controlled by spring surface warming. *Nat. Geosci.* **14**, 912–917 (2021).

26. N. L. Ingraham, B. E. Taylor, Light stable isotope systematics of large‐scale hydrologic regimes in California and Nevada. *Water Resour. Res.* **27**, 77–90 (1991).

27. J. M. Welker, Isotopic (δ18O) characteristics of weekly precipitation collected across the USA: an initial analysis with application to water source studies. *Hydrol. Process.* **14**, 1449–1464 (2000).

28. K. Rozanski, L. Araguás-Araguás, R. Gonfiantini, "Isotopic Patterns in Modern Global Precipitation" in *Climate Change in Continental Isotopic Records* (American Geophysical Union (AGU), 1993; https://onlinelibrary.wiley.com/doi/abs/10.1029/GM078p0001), pp. 1–36.

29. J. Zhu, X.-Z. Liang, Impacts of the Bermuda High on Regional Climate and Ozone over the United States. *J. Clim.* **26**, 1018–1032 (2013).

30. C. Sun, T. M. Shanahan, J. Partin, Controls on the Isotopic Composition of Precipitation in the South-Central United States. *J. Geophys. Res. Atmospheres* **124**, 8320–8335 (2019).

31. F. Song, Z. Feng, L. R. Leung, R. A. H. Jr, J. Wang, J. Hardin, C. R. Homeyer, Contrasting Spring and Summer Large-Scale Environments Associated with Mesoscale Convective Systems over the U.S. Great Plains. *J. Clim.* **32**, 6749–6767 (2019).

32. F. Song, L. R. Leung, J. Lu, L. Dong, Future Changes in Seasonality of the North Pacific and North Atlantic Subtropical Highs. *Geophys. Res. Lett.* **45**, 11,959-11,968 (2018).

33. W. Zhou, L. R. Leung, F. Song, J. Lu, Future Changes in the Great Plains Low-Level Jet Governed by Seasonally Dependent Pattern Changes in the North Atlantic Subtropical High. *Geophys. Res. Lett.* **48**, e2020GL090356 (2021).

34. A. Brauer, G. H. Haug, P. Dulski, D. M. Sigman, J. F. W. Negendank, An abrupt wind shift in western Europe at the onset of the Younger Dryas cold period. *Nat. Geosci.* **1**, 520–523 (2008).

35. F. S. R. Pausata, C. Li, J. J. Wettstein, M. Kageyama, K. H. Nisancioglu, The key role of topography in altering North Atlantic atmospheric circulation during the last glacial period. *Clim. Past* **7**, 1089–1101 (2011).

36. L. M. Baldini, F. McDermott, J. U. L. Baldini, P. Arias, M. Cueto, I. J. Fairchild, D. L. Hoffmann, D. P. Mattey, W. Muller, D. C. Nita, R. Ontanon, C. Garcia-Monco, D. A. Richards, Regional temperature, atmospheric circulation, and sea-ice variability within the Younger Dryas Event constrained using a speleothem from northern Iberia. *Earth Planet. Sci. Lett.* **419**, 101–110 (2015).

37. D. Fastovich, J. M. Russell, S. T. Jackson, T. R. Krause, S. A. Marcott, J. W. Williams, Spatial fingerprint of Younger Dryas cooling and warming in eastern North America. *Geophys. Res. Lett.* **47**, e2020GL090031 (2020).

38. D. McGee, E. Moreno-Chamarro, B. Green, J. Marshall, E. Galbraith, L. Bradtmiller, Hemispherically asymmetric trade wind changes as signatures of past ITCZ shifts. *Quat. Sci. Rev.* **180**, 214–228 (2018).

39. N. El bani Altuna, M. M. Ezat, L. Smik, F. Muschitiello, S. T. Belt, J. Knies, T. L. Rasmussen, Sea ice-ocean coupling during Heinrich Stadials in the Atlantic–Arctic gateway. *Sci. Rep.* **14**, 1065 (2024).

40. H. Bong, A. N. LeGrande, S. Dee, J. Zhu, A. Cauquoin, R. P. Fiorella, Q. Ding, N. Dutrievoz, M. Tanoue, M. Frazer, M. Sarkar, C. Agosta, K. Yoshimura, M. Werner, A. Okazaki, C. Risi, H. C. Steen-Larsen, M. Casado, S. Wahl, J. Nusbaumer, J. Worden, S. Good, A. Bailey, M. Schneider, S. Noël, S. Mandal, K. Bowman, Y. Li, G. A. Schmidt, Water Isotope Model Intercomparison Project (WisoMIP): Present-Day Climate. *J. Geophys. Res. Atmospheres* **131**, e2025JD044985 (2026).

41. B. L. Otto-Bliesner, E. C. Brady, J. Fasullo, A. Jahn, L. Landrum, S. Stevenson, N. Rosenbloom, A. Mai, G. Strand, Climate Variability and Change since 850 CE: An Ensemble Approach with the Community Earth System Model. *Bull. Am. Meteorol. Soc.* **97**, 735–754 (2016).

42. S. Stevenson, B. L. Otto-Bliesner, E. C. Brady, J. Nusbaumer, C. Tabor, R. Tomas, D. C. Noone, Z. Liu, Volcanic Eruption Signatures in the Isotope-Enabled Last Millennium Ensemble. *Paleoceanogr. Paleoclimatology* **34**, 1534–1552 (2019).

43. C. He, “Deciphering the Deglacial Evolution of Water Isotope and Climate in the Northern Hemisphere,” thesis, The Ohio State University, United States -- Ohio (2021).

44. D. A. Bishop, A. P. Williams, R. Seager, Increased fall precipitation in the southeastern United States driven by higher-intensity, frontal precipitation. *Geophys. Res. Lett.* **46**, 8300–8309 (2019).

45. A. G. Pendergrass, D. L. Hartmann, Changes in the Distribution of Rain Frequency and Intensity in Response to Global Warming. *J. Clim.* **27**, 8372–8383 (2014).

46. N. Teale, D. A. Robinson, Long-term variability in atmospheric moisture transport and relationship with heavy precipitation in the eastern USA. *Clim. Change* **175**, 1 (2022).

47. W. Li, L. Li, M. Ting, Y. Liu, Intensification of Northern Hemisphere subtropical highs in a warming climate. *Nat. Geosci.* **5**, 830–834 (2012).

48. D. Fastovich, T. Bhattacharya, S. Jackson, T. Krause, J. Russell, T. Shanahan, C. Sun, J. Williams, Code and Data for Deglacial reconstruction of the spatial extent and intensity of the North Atlantic Subtropical High, version 1, Zenodo (2026); https://doi.org/10.5281/ZENODO.20628395.

49. E. B. B. Otto-Bliesner, R. Tomas, Z. Liu, C. He, iTraCE (2021). https://doi.org/10.26024/b290-an76.

50. B. Otto-Bliesner, E. Brady, J. Fasullo, A. Jahn, L. Landrum, S. Stevenson, N. Rosenbloom, A. Mai, W. Strand, CESM1 Last Millennium Ensemble, NSF National Center for Atmospheric Research (2025); https://doi.org/10.5065/C32Y-RK84.

51. T. R. Krause, J. M. Russell, R. Zhang, J. W. Williams, S. T. Jackson, Late-Quaternary vegetation, climate, and fire history of the Southeast Atlantic Coastal Plain based on a 30,000-yr multi-proxy record from White Pond, South Carolina (USA). *Quat. Res.* **https://doi.org/10.1017/qua.2018.95** (2019).

52. T. R. Krause, J. M. Russell, R. Zhang, J. W. Williams, S. T. Jackson, Late Quaternary vegetation, climate, and fire history of the Southeast Atlantic Coastal Plain based on a 30,000-yr multi-proxy record from White Pond, South Carolina, USA. *Quat. Res.*, 1–20 (2019).

53. J. E. Tierney, F. S. R. Pausata, P. B. deMenocal, Rainfall regimes of the Green Sahara. *Sci. Adv.* **3**, e1601503 (2017).

54. G. J. Bowen, Gridded maps of the isotopic composition of meteoric waters, (2025).

55. M. Blaauw, J. A. Christen, Flexible paleoclimate age-depth models using an autoregressive gamma process. *Bayesian Anal.* **6**, 457–474 (2011).

56. J. Hu, J. Emile-Geay, J. Nusbaumer, D. Noone, Impact of Convective Activity on Precipitation δ18O in Isotope-Enabled General Circulation Models. *J. Geophys. Res. Atmospheres* **123**, 13,595-13,610 (2018).

57. Y. Zhou, L. E. Lisiecki, S. R. Meyers, T. Lee, C. Lawrence, Global and regional Pleistocene benthic $\delta^{18}O$ stacks with a comparison of different age modeling strategies. *Geochronology* **8**, 85–107 (2026).

58. N. Davtian, E. Bard, A new view on abrupt climate changes and the bipolar seesaw based on paleotemperatures from Iberian Margin sediments. *Proc. Natl. Acad. Sci.* **120**, e2209558120 (2023).

Supplemental Figures

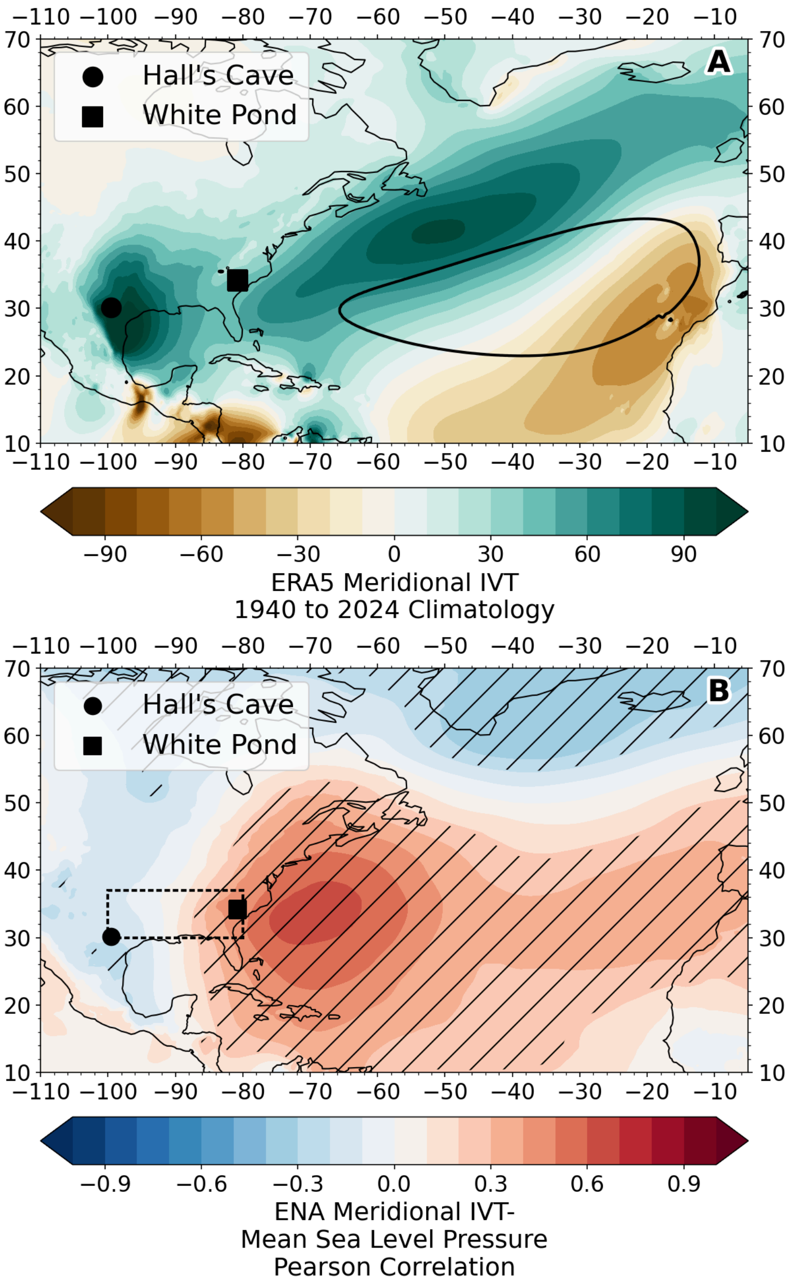

Figure S1. (A) The 1940 to 2024 climatology of meridional integrated vapor transport in southeastern North America and the 1019 hPa isobar (black contour) from ERA5 . (B) The Pearson correlation between meridional integrated vapor transport into southeastern North America (black dashed box) and mean sea level pressure. Regions with significant correlations are denoted with hashing. Significant correlations over the Atlantic suggest that the geostrophic balance between the North Atlantic Subtropical High and low pressure over eastern North America drive meridional moisture flux into southeastern North America.

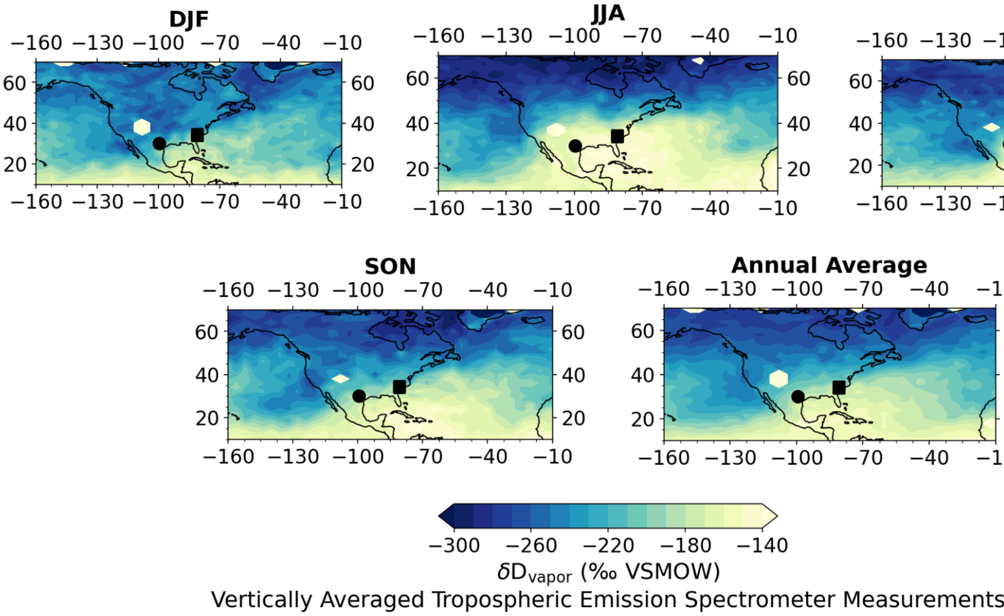

Figure S2. Seasonal and annual climatology of δD_{vapor} from the tropospheric emission spectrometer. Estimates are pressure-weighted and averaged between 825 and 450 hPa. The square and circle points correspond to White Pond and Hall's Cave, respectively. Post-processed data is from (*22*).

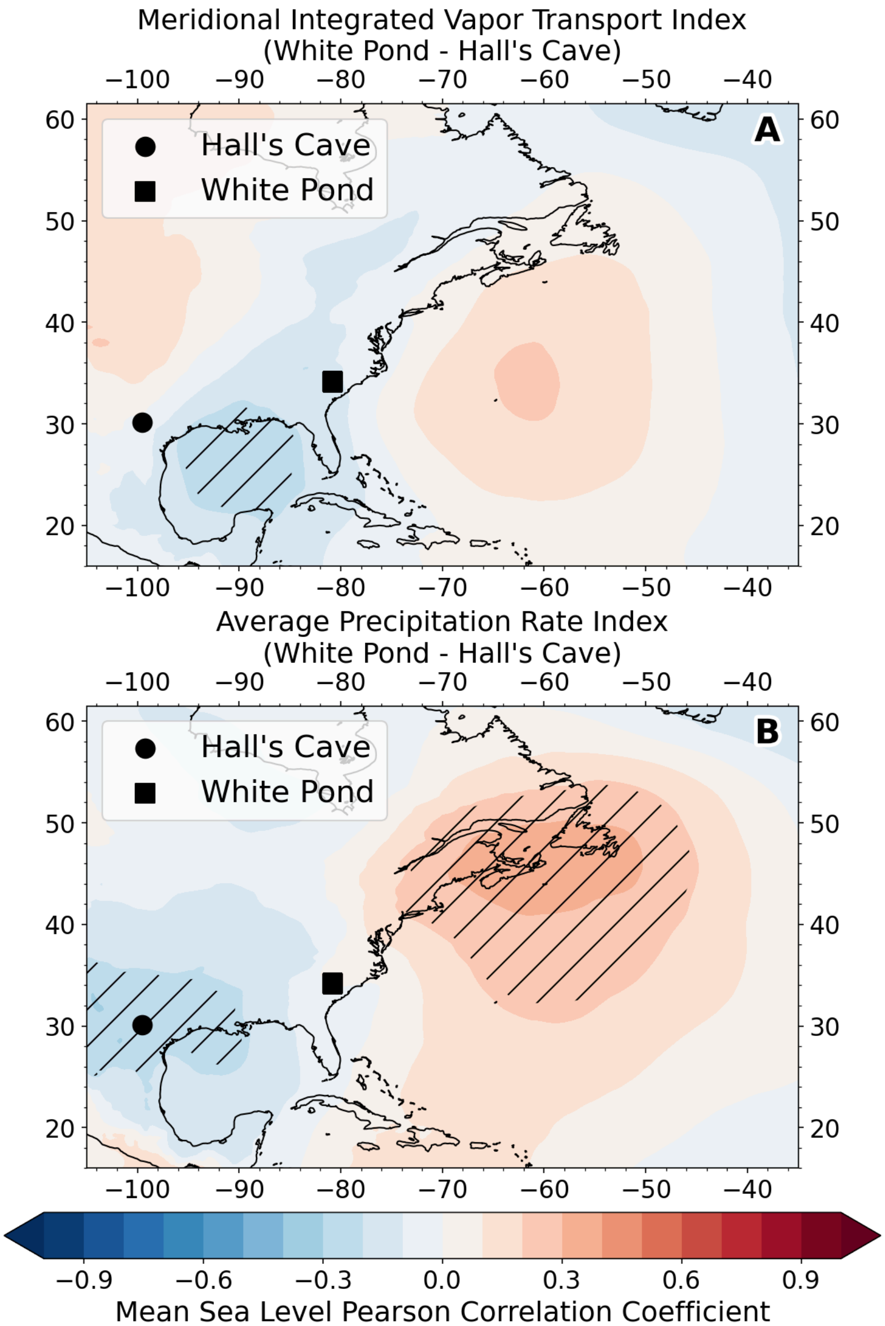

Figure S3. (A, B) The filled contours correspond to the Pearson correlation between indices that replicate ΔδD NASH, but with meteorological fields from ERA5. (A) The standardized difference between meridional integrated vapor transport at White Pond and Hall's Cave is compared to mean sea level pressure. Regions with significant correlations are denoted with hashing. Significant correlations over the Gulf of Mexico suggest that westward expansions in the North Atlantic Subtropical High are correlated with the difference in meridional integrated vapor transport between our two sites. (B) The standardized difference between average precipitation rate at White Pond and Hall's Cave is compared to mean sea level pressure. Regions with significant correlations are denoted with hashing. Significant correlations over the Atlantic suggest that the intensity of the North Atlantic Subtropical High is correlated with the difference in average precipitation rate between our two sites.

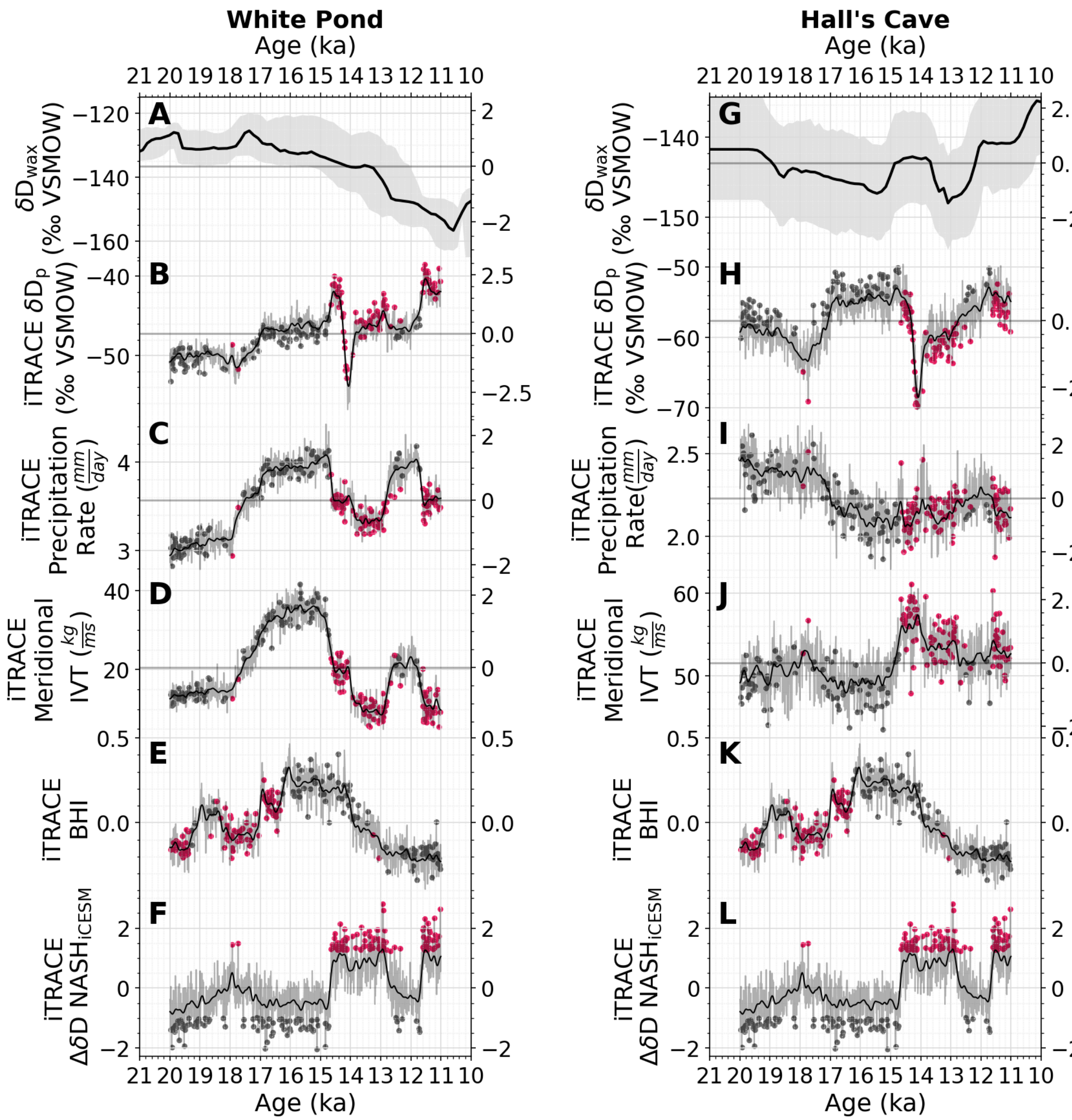

Figure S4. Measured δD_{wax} from (A) White Pond and (G) Hall's Cave with temporal and measurement uncertainty propagated through a resampling approach compared to simulated, iTRACE, time series of site-level (B, H) δD_p, (C, I) precipitation rate, and (D, J) meridional integrated vapor transport. (E, K) Simulated BHI from iTRACE. (F, L) $\Delta\delta D$ $NASH_{iCESM}$ calculated identically to $\Delta\delta D$ $NASH_{leaf\ wax}$. In all iTRACE panels (B-F, H-L), the pink points correspond to time periods when $\Delta\delta D$ $NASH_{iCESM} \geq$ 90th percentile. The gray points correspond to time periods when $\Delta\delta D$ $NASH_{iCESM} \leq$ 10th percentile. Except for (A) and (G), the light gray line corresponds to decadal averages and the dark lines correspond to a Gaussian low-pass filter (σ = 50 years). In A-D and G-J, the right y-axis corresponds to standardized values with the horizontal line representing standardized values of 0.

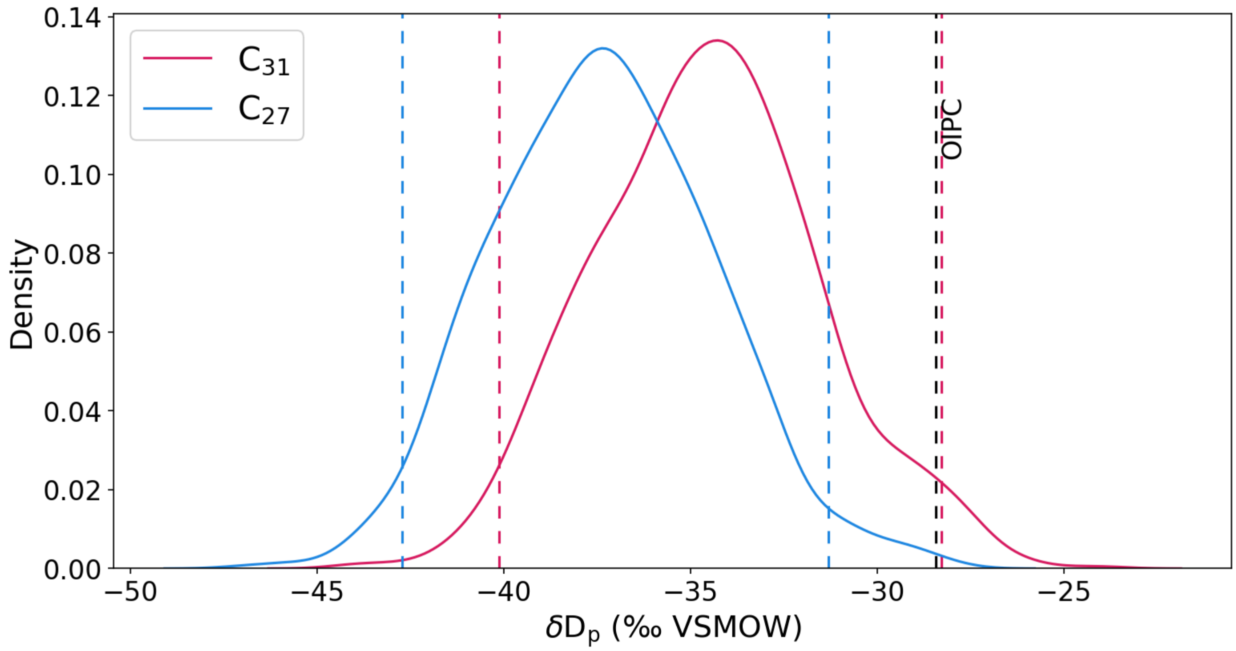

Figure S5. The posterior distribution of predicted δD_p for core top sediment from White Pond where predictions are from a two-end member Bayesian mixing model (*53*). δD_p was reconstructed for C_{31} and C_{27} leaf waxes, with C_{31} showing a closer agreement to observations from the Online Isotopes in Precipitation Calculator. The colored dashed lines correspond to the 95% confidence interval for reconstructed δD_p. The second dashed line near -28‰ for C_{31} is near the black dashed line. The black dashed line corresponds to δD_p for the closet grid cell to White Pond from the Online Isotopes in Precipitation Calculator (*54*).

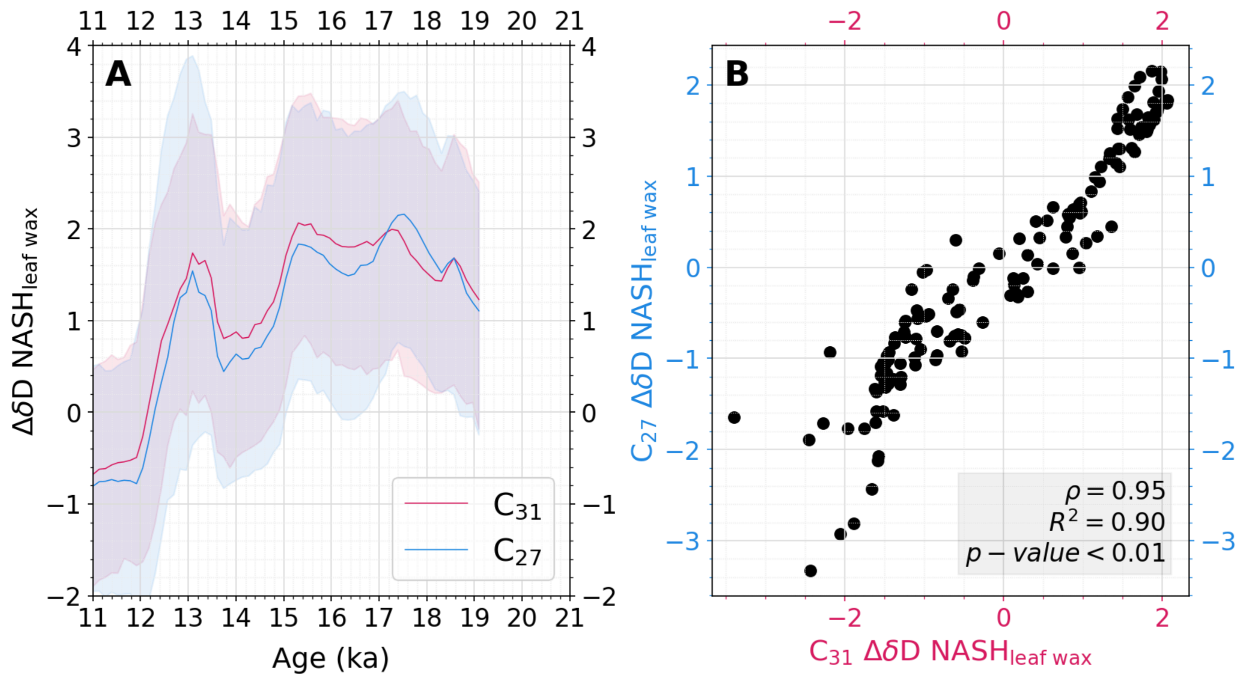

Figure S6. (A) A comparison of North Atlantic Subtropical High reconstructions using C_{31} (pink) and C_{27} (blue) chain length alkanes from White Pond and C_{27} alkanes from Hall's Cave. (B) A crossplot of paired North Atlantic Subtropical High reconstructions from (A). Note the high similarity between reconstructions and high correlation. This suggests that our North Atlantic Subtropical High reconstruction is not sensitive to our analytical decision to focus on C_{31} alkanes at White Pond.

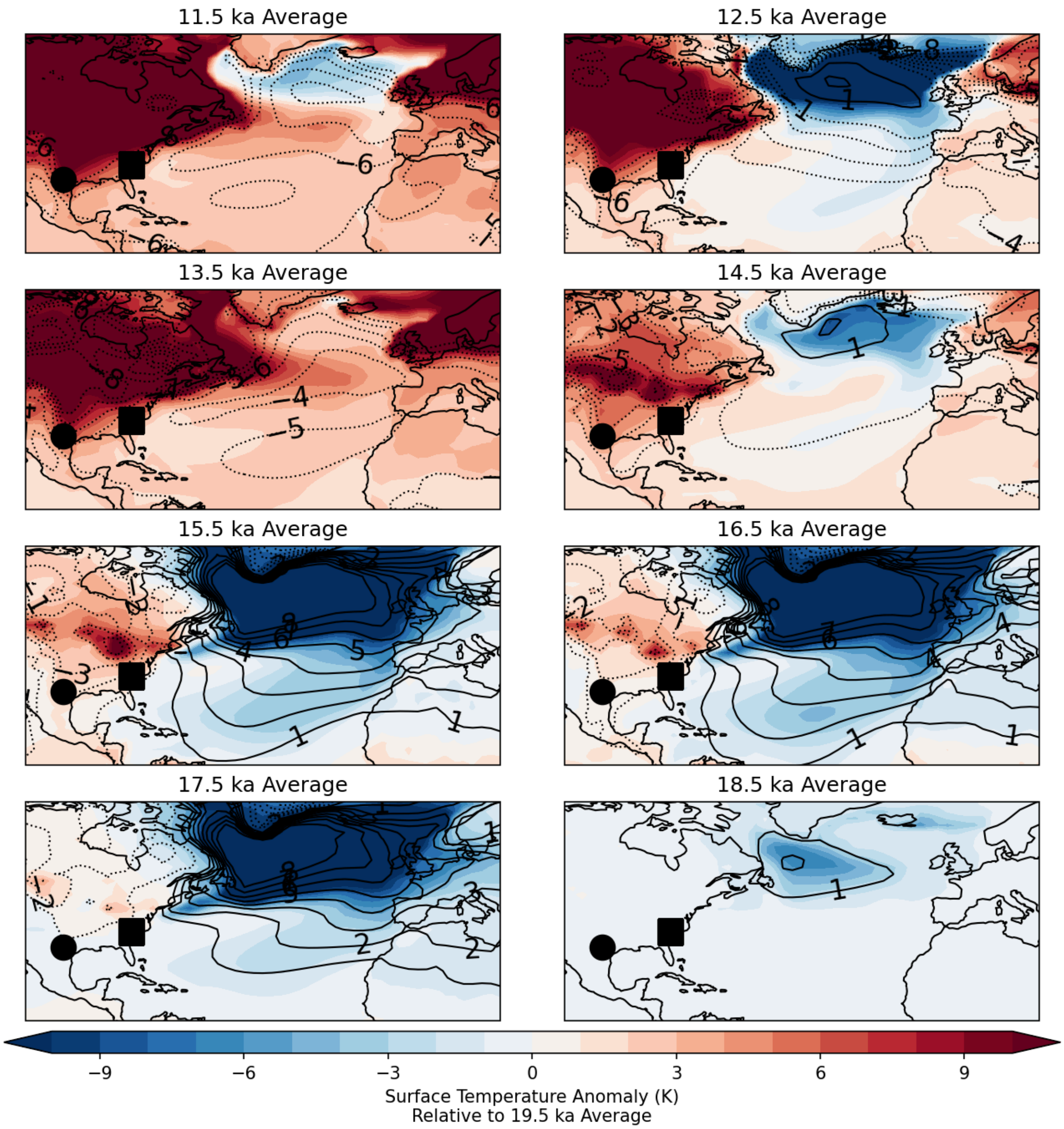

Figure S7. Millennial averages of surface temperature and mean sea level pressure relative to a Last Glacial Maximum baseline (20 to 19 ka). The square and circle points correspond to White Pond and Hall's Cave, respectively.

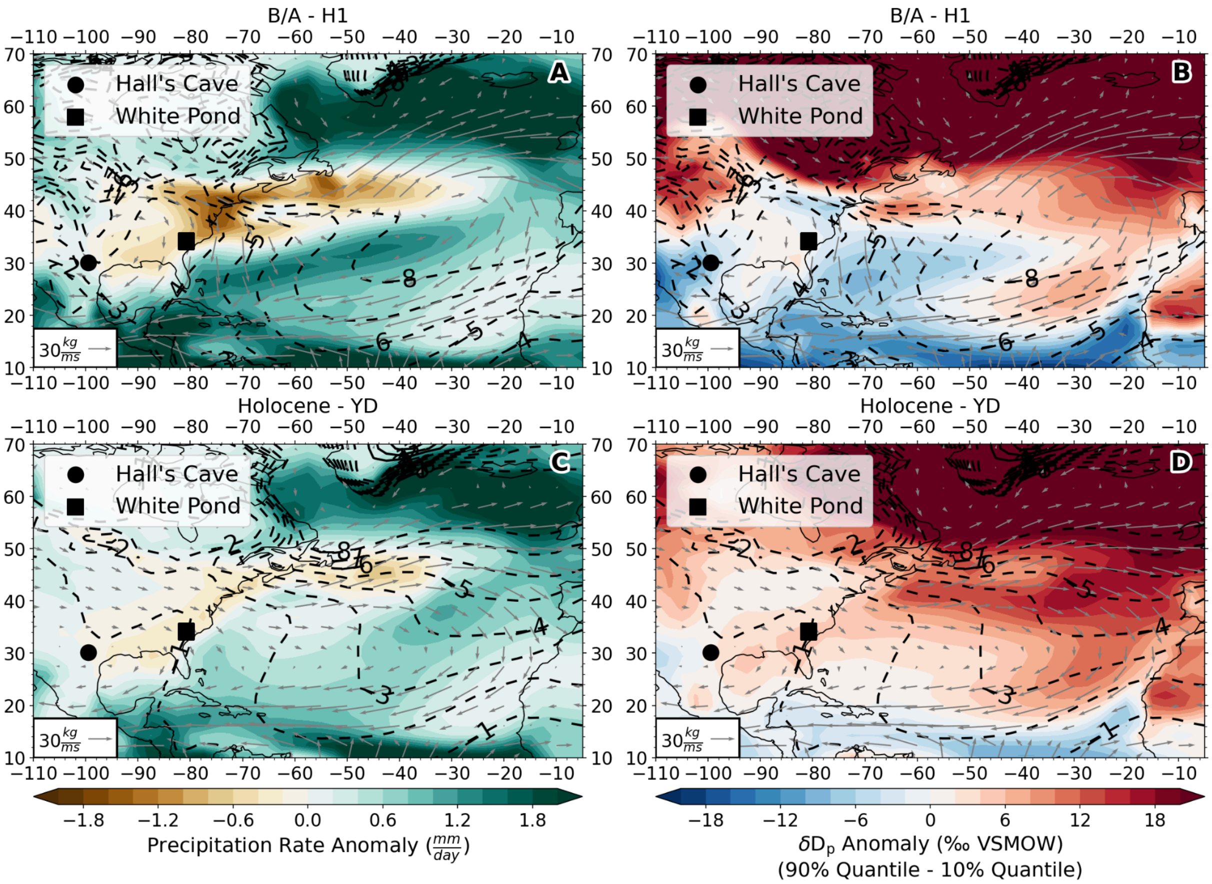

Figure S8. Anomaly fields of simulated (A, C) precipitation rate (filled contours), (B, D) δD_p, (A-D) integrated vapor transport, and (A-D) mean sea level pressure diagnosing the causes of the inverse southeastern North American δD_p gradient-North Atlantic Subtropical High relationship in iTRACE. (A, B) The Heinrich event 1 (temporal average from 17 ka to 15 ka) is subtracted from the Bølling-Allerød (temporal average from 14 ka to 13 ka). Large positive precipitation anomalies in the subtropical and tropical Atlantic from a northward shift in the Intertropical Convergence Zone correspond with decreases in δD_p from the 'amount effect'. Low subtropical and tropical Atlantic δD_p is transmitted to Hall's Cave through easterly anomalies in integrated vapor transport despite decreases in mean sea level pressure. (C, D) The Younger Dryas (temporal average from 12.9 ka to 11.7 ka) is subtracted from the Holocene (temporal average from 11.7 ka to 11 ka, when the iTRACE experiment ends). The spatial patterns in (C, D) mirror (A, B).

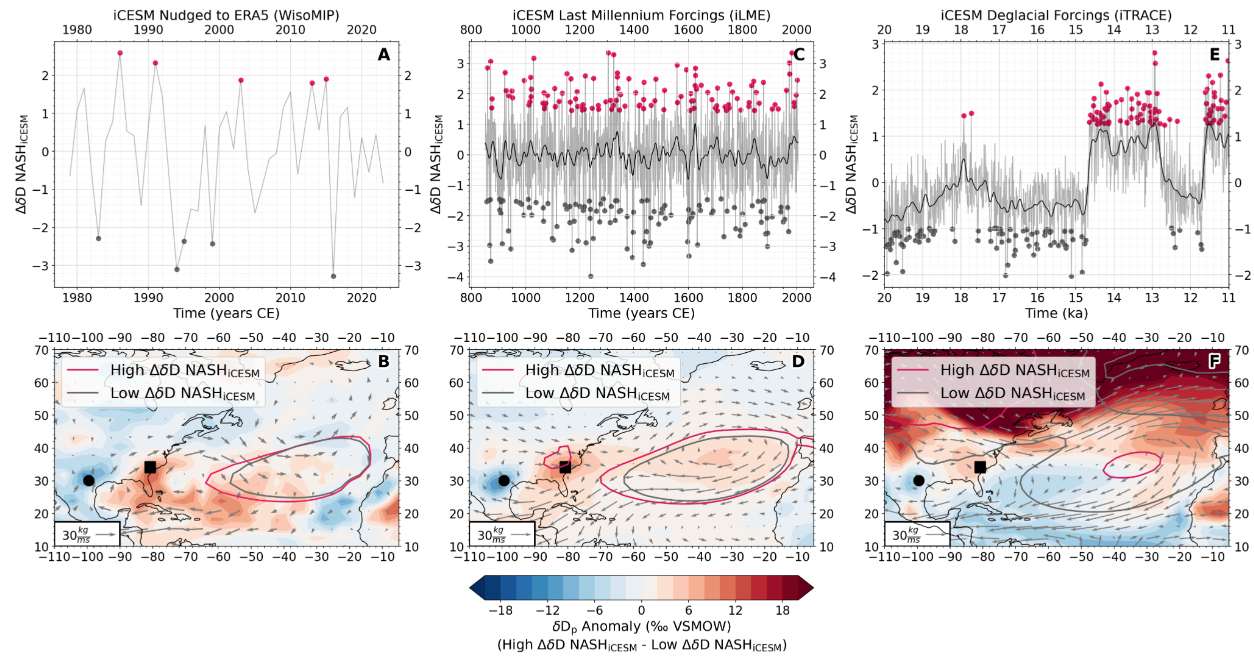

Figure S9. (B, D, F) As in Figure 4, but with the corresponding simulated North Atlantic ΔδD $NASH_{iCESM}$ time series (A, C, E). The pink points correspond to time periods when ΔδD $NASH_{iCESM} \geq$ 90th percentile. The gray points correspond to time periods when ΔδD $NASH_{iCESM}$. The anomaly fields in B, D, and F represent the difference in the average of the pink and gray points from A, C, and E and are identical to Figure 3.

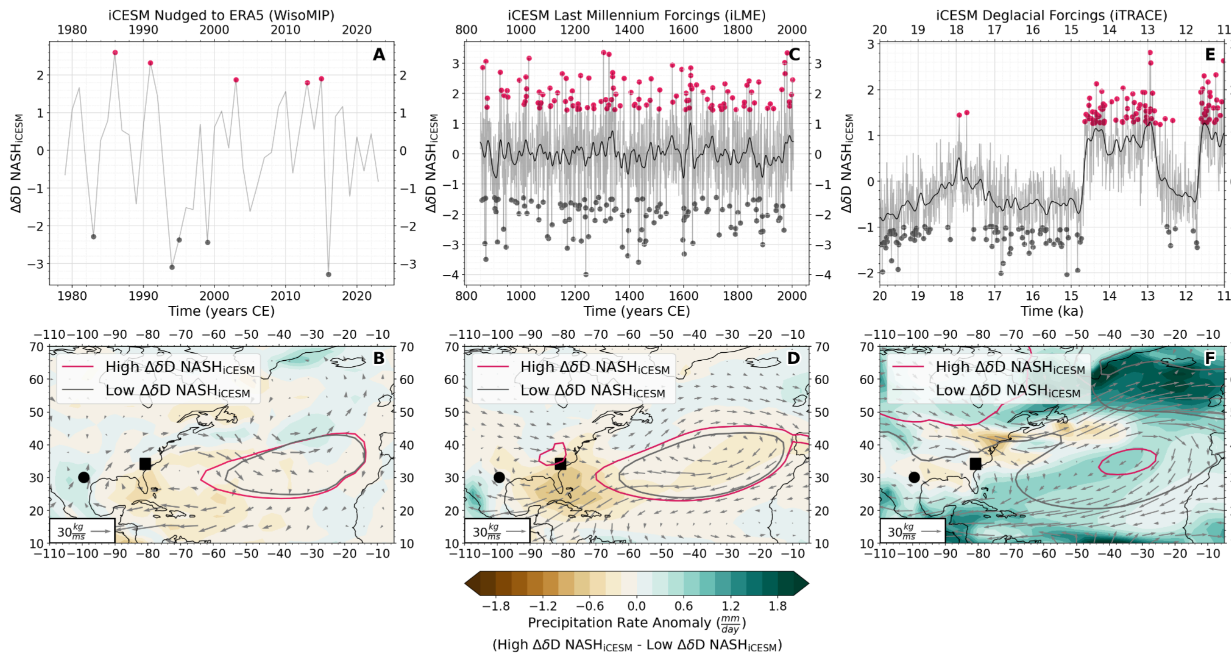

Figure S10. (B, D, F) As in Figure S9 but for simulated precipitation rate anomalies.

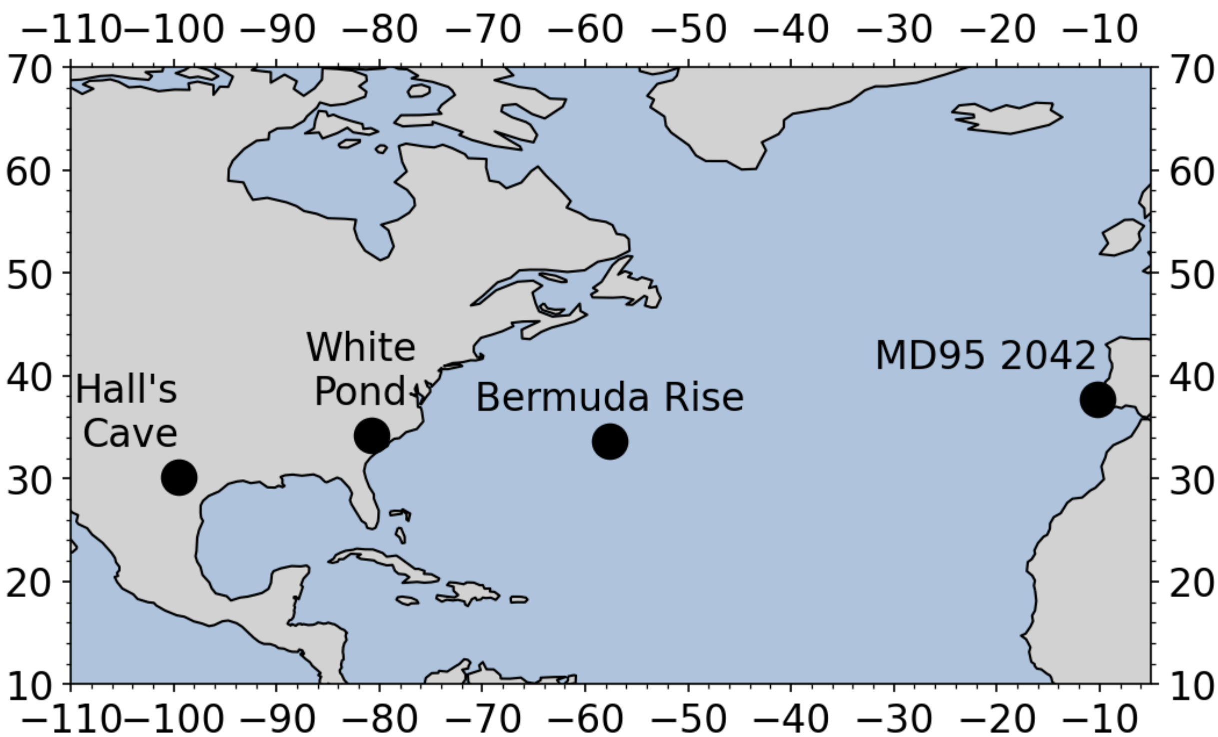

Figure S11. A map of all sites used for analyses in Figures 2 and 4.